BNL-229724-2026-JAAM

Stable Co-valorization of Carbon Dioxide and Methane via Dynamic Reconstruction of a Metal Oxide Solid Solution Catalyst

J. Zhang, J. Boscoboinik

To be published in "ACS Catalysis"

January 2026

Center for Functional Nanomaterials

Brookhaven National Laboratory

U.S. Department of Energy

USDOE Office of Science (SC), Basic Energy Sciences (BES). Scientific User Facilities (SUF)

DISCLAIMER

Stable Co-valorization of Carbon Dioxide and Methane via Dynamic Reconstruction of a Metal Oxide Solid Solution Catalyst

Junyan Zhang[1, θ], Meijia Li[1, θ], Yuanyuan Li[1], Nabihan B. Abdul Rahman[1], Hailing Yu[2], Kevin Siniard[2], Alexander S. Ivanov[1], Xin Wang[1], Harry M. Meyer III[1], Shize Yang[3], Leighanne C. Gallington[4], Victoria Cooley[4], J. Anibal Boscoboinik,[5] Zili Wu[1, 6], Zhenzhen Yang[1, *], Felipe Polo-Garzon[1, *], and Sheng Dai[1, 2, *]

[1]Chemical Sciences Division, Oak Ridge National Laboratory, Oak Ridge, TN 37831, USA
[2]Department of Chemistry, University of Tennessee Knoxville, Knoxville, TN 37996, USA
[3]Aberration Corrected Electron Microscopy Core, Yale University, New Haven, CT 06516, USA
[4]X-Ray Science Division, Advanced Photon Source, Argonne National Laboratory, Lemont, IL 60439, USA
[5]Center for Functional Nanomaterials, Brookhaven National Laboratory, Upton, New York 11973, USA
[6]Center for Nanophase Materials Sciences, Oak Ridge National Laboratory, Oak Ridge, TN 37831, USA

ABSTRACT

Dry reforming of methane (DRM) is a process that converts two greenhouse gases (methane and carbon dioxide) into syngas, a mixture of H_2 and CO, that can lead to a variety of value-added chemicals. Owing to its endothermic nature, high reaction temperatures up to 800 °C are typically required and the grand challenge lies in developing robust catalysts without sintering and coking-induced deactivation during the long-term on-stream operation. Towards this aim, herein, a robust complex oxide-supported NiCu alloy catalyst was generated in situ during DRM. By leveraging the configurational stability of a solid oxide solution precursor, tightly anchored NiCu bimetallic nanoparticles were in situ exsoluted and acted as the active sites in DRM. The as-afforded catalyst exhibited stable performance for DRM due to the ability to repel coke off the surface as the reaction proceeds. Kinetic experiments along with top surface characterization detail the reconstruction behavior of the solid oxide solution under DRM reaction conditions. The fundamental insights from this work provide guidance on generating resistant and flexible catalysts via in situ active sites formation from easily synthesized metal oxide solid solutions.

KEYWORDS

Dry reforming of methane • Solid solution catalyst • Complex metal oxide • Exsolution • NiCu alloy

INTRODUCTION

The shale gas revolution has significantly boosted natural gas supply, providing an abundant source of methane for cost-effective hydrogen production.[1] Currently, methane is mainly converted to hydrogen through steam reforming, a process that is highly energy-intensive and consumes substantial amounts of water.[2, 3] In contrast, dry reforming of methane (DRM) offers an alternative route for hydrogen production that is independent of water resources.[4-8] Further, this chemical process utilizes two major greenhouse gases, methane (CH_4) and carbon dioxide (CO_2), thereby contributing to address the challenges of climate change associated with greenhouse gas emissions.[3, 9] For decades, transition-metal-supported catalysts have been tested for DRM, yet DRM has not been industrially adopted because of catalyst deactivation during reaction.[10] Due to the endothermic nature of the reaction, it requires temperatures above 600 °C for significant conversion of both CH_4 and CO_2.[11] This high temperature promotes catalyst deactivation due to

sintering of metal sites, leading to the loss of active sites. Meanwhile, the larger particle size after sintering can also accelerate coke deposition from methane decomposition and the Boudouard reaction.[12]

Ni-MgO catalysts are among the most extensively studied catalysts for DRM. NiO has been dissolved in a MgO matrix to form a homogeneous phase.[10, 13] Although these catalysts are susceptible to deactivation during the reaction, several strategies have been designed to extend their lifetime, including tuning synthesis conditions, particle size, surface properties, and pretreatment conditions. It was demonstrated that the incomplete formation of the solid solution at lower temperatures (500 °C) leads to rapid deactivation, and synthesis at temperatures above 700 °C result in the formation of larger particles with lower reducibility, hence reduced reactivity.[14] An intermediate calcination temperature around 600 °C facilitated complete mixing of Ni and Mg oxides with proper interactions, showing high resistance to deactivation. Utilization of MgO nanocrystal supports with small particle size has been shown to extend catalyst lifetime during DRM.[15, 16] NiO species loaded onto MgO nanocrystals ranging from 7–17 nm via impregnation exhibited minimal deactivation at 757–790 °C, with defect-rich MgO surfaces providing abundant anchoring sites for Ni.[16] More recently, deposition of Ni-Mo bimetallic nanoparticles (NPs) onto a MgO support devoid of surface groups produced the "Nanocatalysts On Single Crystal Edges" (NOSCE) effect,[17] where Ni-Mo species aggregate at the vertices of MgO cubes to form ~17 nm alloy NPs, effectively suppressing coke formation and enabling stable DRM. Despite these advances, achieving long-term catalyst stability remains highly challenging, as it requires precise control over precursor composition, particle size, and support morphology.[18, 19] A major gap persists in developing DRM catalysts that combine high stability, scalable synthesis, and robustness under harsh reaction conditions, representing a critical barrier to industrial implementation.

In this work, we tackle the central barrier hindering industrial implementation of DRM, which is the long-term catalyst stability under harsh reaction conditions, by developing a multimetallic solid-solution catalyst with enhanced metal–support interactions (Figure 1A). A $NiMgCuZnO_x$ oxide precursor was synthesized to enable the controlled exsolution of stable Ni–Cu alloy NPs under DRM operation. Other Ni-based multielement oxide catalysts have shown good stability during DRM by leveraging the entropic stabilization effect.[20-22] In our work, the rational component selection ensures synergistic functionality, where Ni–Mg provide a robust catalytic framework, Cu and Zn enhance CO_2 activation while suppressing deep CH_4 decomposition and carbon accumulation, and the similar ionic radii of Ni, Mg, Cu, and Zn facilitate the formation of a homogeneous solid solution with strong lattice integrity. By tuning the configurational entropy of the complex oxide precursor, we achieve controlled and sustained exsolution of Ni–Cu active sites in the reductive DRM environment, thereby preventing sintering-induced deactivation. The resulting $NiMgCuZnO_x$ catalyst demonstrated remarkable stability at 800 °C over 120 h of DRM with equimolar CH_4/CO_2 feed. Detailed characterization confirmed that the catalyst not only generated bimetallic Ni–Cu NPs in situ, but also continued to exsolve additional active sites during operation while simultaneously removing carbon deposits. This dynamic restructuring mechanism effectively mitigates the dual deactivation pathways of sintering and coking, directly addressing the long-standing challenge of stable, scalable, and durable DRM catalysis.

METHODS

Catalyst synthesis

Nickel chloride ($NiCl_2$), magnesium chloride hexahydrate ($MgCl_2 \cdot 6H_2O$), copper chloride ($CuCl_2$), and zinc chloride ($ZnCl_2$) were obtained from Sigma-Aldrich and used without further purification. In a typical synthesis, 0.26 g of $NiCl_2$, 0.406 g of $MgCl_2 \cdot 6H_2O$, 0.27 g of $CuCl_2$, and 0.27 g of $ZnCl_2$ with a molar ratio of 1:1:1:1, were ground using a Retsch ball mill for 2 hours at 30 Hz. Stainless steel milling jars and four stainless steel balls (10 mm in diameter) were used. The resulting mixture was then calcined in a muffle furnace at 900 °C for 4 hours under static air, with a ramp rate of 5 °C min^{-1}.

Catalyst characterization

Ex situ powder X-ray diffraction (XRD) analysis of catalysts was conducted using a PANalytical X′Pert Pro MPD system equipped with an X′Celerator solid-state detector (Cu Kα source, λ=0.1542 nm, 45 kV, 40 mA). Scanning was performed over a wide 2θ range, utilizing a step size of 0.007° and a rate of 0.03° s^{-1}.

In situ high temperature X-ray diffraction (HTXRD) was performed on a Malvern PANalytical Empyrean diffractometer utilizing an Anton Paar HTK 1200N high-temperature chamber and a Cu LFF HR X-ray tube. Diffraction patterns from 20 to 85 ° (2θ) were obtained with a step size of 0.0394 ° and a scan speed of approximately 0.32 °/sec (0.14 °/sec for in situ XRD under DRM). For in situ XRD under H_2, data were continuously collected as the temperature was ramped from 25 to 900 °C at a rate of 5 °C/min and maintained at 900 °C for 1 h under 2%H_2/N_2 atmosphere. For in situ XRD under DRM reaction conditions, the sample was first pretreated ex situ in 5% O_2/He at 900 °C for 1 h, followed by pretreatment in 30% H_2/Ar at 800 °C for 5 h. Next, the sample was transported to the XRD chamber for in situ measurement. Data were continuously collected as the temperature was ramped at 40 °C/min to 800 °C and maintained at 800 °C for 180 min under a 0.5% CO_2/0.5%CH_4/He (150 cm^3/min) atmosphere.

The nanometer-resolution electron micrographs and EDX maps, high-resolution transmission electron microscopy (HR-TEM) images, were obtained using a Fisher Scientific Spectra 300 aberration-corrected, scanning transmission electron microscope (STEM) operated at 200 KeV. The point resolution in the aberration-corrected mode was 0.08 nm. The microscope was fitted with a SuperXTM X-ray detector, which was a combination of four detectors for fast X-ray mapping in a STEM mode. Nanometer resolution EDX maps were taken at an average beam current of 100 pA. The size of the maps was 512×512 pixels, and 50μs/pixel dwell time was used for collecting the signal. All maps were generated by summing over 10 frames. The drift correction during data collection and subsequent analysis were performed using Velox software.

Temperature-programed reduction (TPR) experiments were performed in an AMI-300 instrument (Altamira Instruments). An amount of 10 mg sample was loaded into a U-shape reactor diluted by 100 mg quartz sand (180-250 μm, Sigma Aldrich) and calcined in 40 cm^3 min^{-1} 5% O_2/He at 900 °C at a ramping rate of 10 °C min^{-1}. After 60 min calcination, the sample was cooled down to 50 °C in 70 cm^3 min^{-1} Ar to remove the residual oxygen. The TPR data was collected with a program-controlled ramping procedure from 50 to 800 °C at 10 °C min^{-1} in 40 cm^3 min^{-1} 4% H_2/Ar and hold at 800 °C for 30 min.

Raman spectroscopy was performed ex situ at room temperature on a multiwavelength Raman system[23] using 244 nm laser excitation (2 mW at sample position). Spectra were collected via a customized ellipsoidal mirror and directed by a fiber optics bundle to the spectrograph stage of a triple Raman spectrometer (Princeton Instruments Acton Trivista 555). To block the laser irradiation, an edge filter (Semrock) was used in front of the UV-vis fiber optic bundle (Princeton Instruments). A UV-enhanced liquid N_2-cooled CCD detector (Princeton Instruments) was employed for signal detection. The samples were analyzed for 60 s on a stationary sample holder.

Temperature-programed oxidation (TPO) was conducted on a commercial AMI-300 instrument (Altamira Instruments, Inc). For the TPO of whole catalysts bed (catalyst + dilution), the U-shape rector after reaction was flushed with 40 cm^3 min^{-1} Ar for 1h and 40 cm^3 min^{-1} 5% O_2/He for 0.5 h at 50 °C, followed by ramping to 900 °C at 10 °C min^{-1}. To quantify the coke deposited only on the catalyst (not the quartz wool and sand), the spent $NiMgCuZnO_x$ was separated from the quartz sand with a Neodymium magnet. After loading into a clean U-shape reactor with fresh quartz sand and wool, the TPO was performed with the same procedure.

Temperature-programed CO_2 desorption (CO_2-TPD) experiments were performed in an AMI-300 instrument. 10 mg sample was loaded into a U-shape reactor diluted by 100 mg quartz sand (180-250 μm, Sigma Aldrich). The catalyst pretreatment steps were similar to those outlined in the DRM reaction procedures. After the final Ar flush during the pretreatment phase, the catalyst was cooled down to 50 °C under 40 cm^3 min^{-1} Ar and the temperature was allowed to stabilize for 30 mins. Once stabilized, the catalyst was exposed to 40 cm^3 min^{-1} of 10% CO_2/Ar for 30 mins, which then flushed under 40 $cm^3 min^{-1}$ Ar for 2

hours to remove excess physiosorbed CO_2. The TPD data was collected with a program-controlled ramping procedure from 50 to 900 °C at 10 °C min^{-1} in 40 cm^3 min^{-1} Ar and hold at 800 °C for 30 min.

The metal contents of the catalysts were determined by inductively coupled plasma atomic emission spectroscopy (ICP-AES) with the Optima 7000DV instrument from PerkinElmer, USA.

Diffuse reflectance infrared Fourier transform spectroscopy (DRIFTS) was conducted on a Nicolet Nexus 670 spectrometer with an MCT detector. CO was sourced from a gas cylinder containing a 2% CO/He mixture. CaF_2 was blended with the sample to enhance the signal intensity with weight ratio of 3:1. Typically, around 5 mg of mixture was placed into a porous ceramic cup within the DRIFTS cell (Pike technologies) followed by pretreatment. Before DRIFTS experiments, the as-synthesized sample was calcined in situ at 500 °C (10 °C min^{-1} ramping rate) under 30 cm^3 min^{-1} 3.5 % O_2 (balanced with Ar) and held for 1 h. The reduced samples was treated ex situ (first calcined with 40 cm^3 min^{-1} 5% O_2/He at 900 °C for 1h, followed by Ar flush, and then treated in 40 cm^3 min^{-1} 30% H_2/Ar at 800 °C for 5 h) and then in situ in 30 cm^3 min^{-1} 4% H_2/Ar at 500 °C for 1 h. The 80 h spent sample was treated in situ in 30 cm^3 min^{-1} Ar at 400 °C for 1 h. After in situ pretreatment, the sample cell was purged with 30 cm^3 min^{-1} of Ar to evacuate any residual oxidative or reductive gas and then cooled to -100 °C. After reaching -100 °C, the background spectra were collected before introducing CO. 0.67% CO gas (balanced by inert) was flowed for 5 min followed by flushing with 30 cm^3 min^{-1} Ar for 5 min. The spectra was collected in 10 s interval.

Ex situ X-ray photoelectron spectroscopy (XPS) experiments were carried out in a Thermo Scientific (Waltham, MA, USA) Model K-Alpha XPS instrument, which utilizes monochromated, micro-focused, Al K_α X-rays (1486.6 eV) with a variable spot size (i.e., 30-400 µm). Analyses of the samples were performed with a 400 µm X-ray spot size. The instrument has a hemispherical electron energy analyzer equipped with a 128-channel detector system. Base pressure in the analysis chamber typically reaches 2 x 10^{-9} mbar or lower. Samples were prepared for analysis by dispersing the catalyst powder onto double-sided tape fixed to a clean glass slide. Survey spectra (pass energy = 200 eV) were acquired for qualitative and quantitative analysis and high-resolution core level spectra (pass energy = 50 eV) were acquired for detailed chemical characterization. A charge neutralization flood gun was used to maintain a stable analysis condition. The typical pressure in the analysis chamber with the flood gun operating is 2 x 10^{-7} mbar. Data were collected and processed using the Thermo Scientific Avantage XPS software package (v.5.96). Peak fitting was performed using mixed Gaussian/Lorentzian peak shapes and a Shirley/Smart type background.

Near-ambient pressure XPS (NAP-XPS) experiments were performed at the Center for Functional Materials at Brookhaven National Laboratory equipped with a lab-based APXPS system (SPECS Surface Nano Analysis). A monochromatized Al Kα X-ray source (hv = 1486.6 eV), focused to a ca. 300 µm diameter spot size and fixed at 55° from the sample normal, and a differentially pumped hemispherical analyzer were used for acquiring XPS spectra. Survey spectra were collected using a pass energy of 50 eV and a step size of 1 eV, and higher-resolution spectra were collected with a 30 eV pass energy. The samples were pressed to a cleaned thin Cu foil, transferred into the main analysis chamber and aligned at a sample to cone distance of 600 µm. Spectra were acquired at the stated conditions of H_2 pressure and temperature. H_2 was delivered to the chamber using a precision variable leak valve and the sample was heated using a IR laser source shining at the bottom of the sample holder. The temperature was measured using a type-K thermocouple attached to the sample. H_2 was introduced before starting the temperature ramp. The ramping rate between temperatures was approximately 20 °C/min. The sample was kept at each temperature for approximately 50 min.

Low-energy ion scattering (LEIS) measurements were performed in an ION-TOF $Qtac^{100}$ spectrometer. The as-synthesized sample was calcined in situ at 400 °C in 5 mbar of O_2 for 1 h. The reduced sample was treated ex situ (first calcined with 40 cm^3 min^{-1} 5% O_2/He at 900 °C for 1h, followed by Ar flush, and then treated in 40 cm^3 min^{-1} 30% H_2/Ar at 800 °C for 5 h) and again treated in situ under 5% H_2/N_2 at 400 °C for 1h. The three spent samples were treated in inert gas at 100 °C for 1 h. Spectra were obtained by applying a 5 keV Ne^+ beam at 2×10^{14} ions/cm^2 per profile cycle. To obtain the depth

profile, samples were sputtered to a depth of approximately 8 nm using an Ar beam (0.5 keV Ar^+ beam at 8×10^{14} ions/cm^2 per profile cycle), and spectra were acquired at each 0.5 nm increment.

The K edge X-ray Absorption Spectroscopy (XAS) spectra of Ni and Cu were measured at NIST beamline 6-BM of National Synchrotron Light Source II at Brookhaven National Laboratory (BNL). All samples were energy calibrated to a respective metal foil reference. All samples were prepared as pellets by mixing with varying amount of boron nitride and contained in polyimide foil. Measurements were performed in transmission mode. The data analysis and reduction process were carried out utilizing the Demeter software suite[24].

Synchrotron X-ray pair distribution function (PDF) scattering measurements were carried out at the 1-ID-C beamline of the Advanced Photon Source (APS), Argonne National Laboratory. Total scattering patterns were collected using a monochromatic 0.173112 Å (71.6 keV) X-ray beam slitted down to a beam size of 200 μm x 200 μm. Two-dimensional patterns were collected in transmission geometry on an amorphous silicon-based area detector (Varex, 2880×2880 pixels, 150 μm pixel pitch) positioned ~500 mm downstream of the sample position. Powder samples were enclosed in thin polyimide capillaries (Cole-Parmer, OD:1.1 mm), sealed from both ends with epoxy, and measured at room temperature. For each sample, 180 frames were collected with 1 s exposure time per frame. Data for an empty polyimide container was also collected to subtract the background signal. Calibration of the sample to detector distance and detector alignment with data from a CeO_2 powder standard was done using GSAS-II.[25] Raw scattering data were radially integrated into *q*-space spectra, applying a mask during integration. The normalized total scattering patterns – structure functions, *S*(*q*)'s were obtained in *PDFgetX3*[26] by subtracting polyimide container scattering, employing the appropriate sample composition, and applying standard corrections for the area detector setup.[27] Pair distribution functions, *G*(*r*), were calculated via Fourier transformation (eq. 1) of the total scattering data with a q_{max} of 20.0 $Å^{-1}$.

$$G(r) = \frac{2}{\pi}\int_{q_{min}}^{q_{max}} q[S(q) - 1]\, sin(qr) dq \qquad (1)$$

Catalyst testing

Dry reforming of methane was conducted on a AMI-300 instrument with a program-controlled procedure. Typically, 15 mg sample was pelletized and sieved to particles size below 45 μm and diluted with 180-250 μm quartz sand with a weight ratio of 1:10, followed by loading into a U-shape quartz rector (inner diameter 4 mm) with a fixed-bed configuration. A K-type thermocouple, covered with quartz sleeve, was located on the top of the catalyst bed for temperature control. Prior to conducting the DRM reaction, the catalysts were calcined with 40 cm^3 min^{-1} 5% O_2/He at 900 °C for 1h. After cooling down to 800 °C, the system was flushed with 40 cm^3 min^{-1} Ar to remove the residual oxygen and helium. After cooling down to 50 °C, the catalyst was reduced with 40 cm^3 min^{-1} 30% H_2/Ar with ramping up to 800 °C and hold for 5 h followed by flushing with 40 cm^3 min^{-1} Ar. For the DRM reaction, 80 cm^3 min^{-1} with composition of 5% CH_4, 5% CO_2 (diluted by Ar) or 50% CH_4, 50% CO_2 was flowed through the catalyst bed. The real-time change of reactants and products were recorded by an online mass spectrometer (MS, Pfeiffer Vacuum). A gas chromatograph (Buck Scientific. Inc) equipped with a thermal conductivity detector (TCD) was utilized for product quantification.

The conversion of CH_4 and CO_2 was calculated using equation (1):

$$X_{reactant} = \frac{C_{inlet} \times F_{inlet} - C_{outlet} \times F_{outlet}}{C_{inlet} \times F_{inlet}} \qquad (1)$$

where $X_{reactant}$ (%) is the conversion for CH_4 and CO_2, C_{inlet} is the concentration of reactant feeding into the reactor, C_{outlet} is the concentration of reactant in product stream, F_{inlet} is the flow rate of the feed and F_{outlet} is the flow rate of the outlet stream.

$$H_2\ to\ CO\ ratio = \frac{C_{H_2,outlet}}{C_{CO,outlet}} \qquad (2)$$

Where $C_{H_2,outlet}$ and $C_{CO,outlet}$ are H_2 and CO concentration in product stream, respectively.

It is worth noting that the severe coke deposition counts for less than 5% of carbon conversion even for the initial 20 h, indicating a decent carbon balance.

Temperature-programmed surface reaction (TPSR) was performed on an AMI-300 instrument. 5 mg of unpelletized spent sample was loaded in the U-shape reactor and diluted with 50 mg quartz sand (180-250 μm) in a fixed-bed configuration. The catalyst bed was flushed with 40 cm^3 min^{-1} Ar at 50 °C before switching to a reactant flow of 80 cm^3 min^{-1} 5 % CH_4, 5% CO_2 balanced with Ar. Then the catalyst bed was heated to 900 °C at 5 °Cmin^{-1}. The products was measured by an online mass spectrometer (MS, Pfeiffer Vacuum).

Chemical looping DRM was performed using the AMI-300 instrument at a temperature of 800 °C. The catalyst mass, particle sizes, and catalyst pretreatment steps were similar to those outlined in the DRM reaction procedures. After the final Ar flush during the pretreatment phase, the first cycle of the chemical looping was commenced. Each cycle consisted of the following sequence: 1) 80 cm^3 min^{-1} of Argon for 15 min, 2) 80 cm^3 min^{-1} of 5% CH_4/Ar for 15 minutes, 3) 80 cm^3 min^{-1} of Argon for 15 min, and 4) 80 cm^3 min^{-1} of 5% CO_2/Ar for 15 min. The real-time change of reactants and products were recorded using an online mass spectrometer (MS, Pfeiffer Vacuum).

RESULTS

Synthesis and characterization of $NiMgCuZnO_x$ solid solution

The four components of the $NiMgCuZnO_x$ solid solution were deployed according to their individual roles in facilitating DRM procedure. Ni-MgO catalysts have shown promising performance for DRM as mentioned above,[10, 13-17] Cu and Zn are metal dopants to enhance DRM performance. NiCu catalysts have shown more stable performance compared to pure Ni, which was attributed to enhanced activation of CO_2 and inhibited CH_4 decomposition.[28-31] NiZn has been suggested as a surface with high reactivity and improved carbon deposition resistance.[32, 33] Our $NiMgCuZnO_x$ catalyst was synthesized via a facile mechanochemical approach followed by calcination at 900 °C (Figure 1A).[34, 35] The as-synthesized catalyst had particle size of approximately 0.5-1.6 μm, and metals were uniformly distributed as shown by elemental mapping via scanning transmission electron microscopy (STEM) (Figure S1). The as-synthesized $NiMgCuZnO_x$ exhibited X-ray diffraction (XRD) patterns corresponding to a rock salt crystal structure (Figure 1B), with no discernible peaks corresponding to secondary phases. To verify the influence of a solid solution formation on reducibility of individual metal components, hydrogen temperature-programmed reduction (H_2 TPR) was employed to assess the reducibility of the Ni and Cu species. As shown in Figure 1C, $NiMgCuZnO_x$ did not show any noticeable reduction peak related to bulk Ni (425 °C) or Cu (275 °C) oxides up to 800 °C. Such an observation supported that the Ni, Mg, Cu and Zn form a solid solution, instead of a physical mixture of individual oxides, with strong interactions that enhance the resistance against uncontrolled reduction of Ni and Cu species.

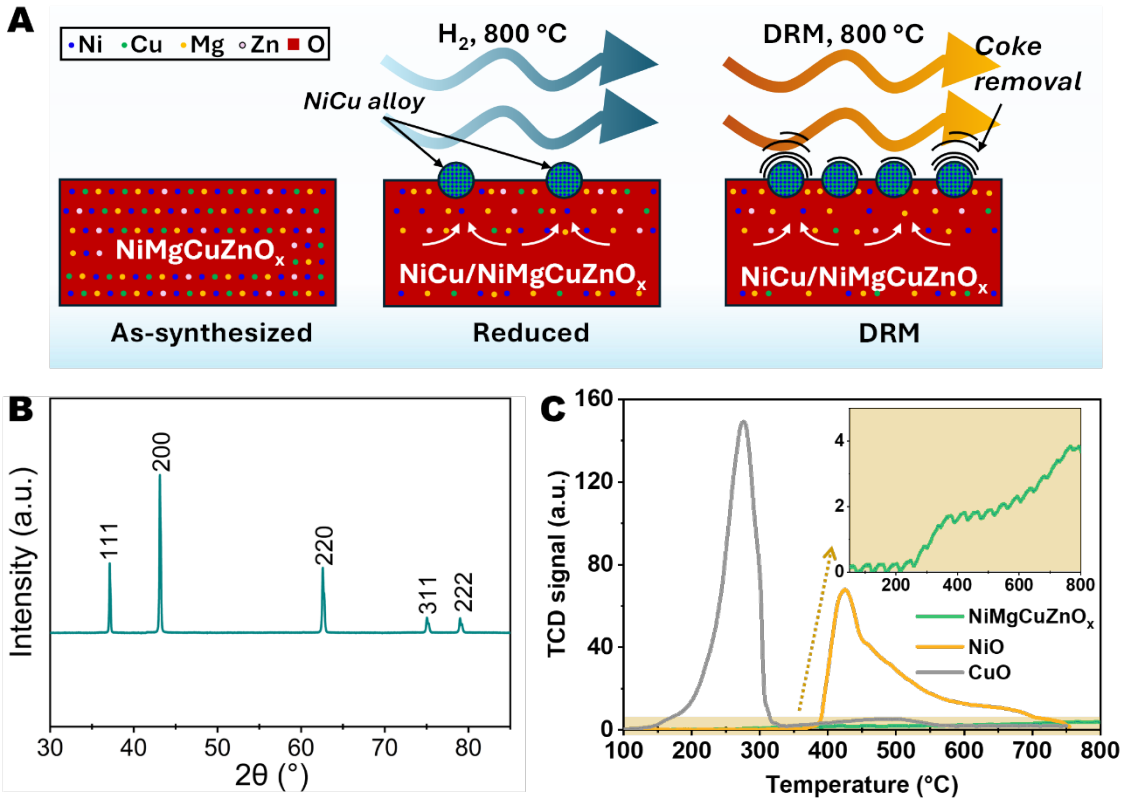

Figure 1. Design principle and characterization of complex metal oxide catalyst.
(A) Schematic of metal oxide solid solution catalyst reconstruction under reducing condition and DRM procedure.

(B) XRD pattern of $NiMgCuZnO_x$ solid solution.

(C) H_2 TPR of as-synthesized $NiMgCuZnO_x$ and $NiMgCuO_x$.

Catalytic performance in DRM and coking resistance

The catalyst was pretreated in situ, first calcined in 5 % O_2 at 900 °C and then reduced in 30% H_2 at 800 °C, prior to conducting DRM at 800 °C using a reactant feed of 50 % CH_4 and 50 % CO_2. Using a concentrated feed was intended to accelerate the reconstruction of the catalyst triggered by the chemical potential of species involved during DRM. Figure 2A shows stable performance of the $NiMgCuZnO_x$ catalyst with prolonged time on stream (TOS) after an initial induction period. The catalyst reached the highest activity after 33 h TOS and deactivated only 8% after 87 h TOS (Figure 2A and 2B). Due to the low conversion, controlled on purpose to show the deactivation trend, the H_2 to CO ratio was around 0.53 owing to the competing reverse water gas shift (RWGS) reaction under relatively high partial pressure of CO_2. Given the apparently enhanced stability by incorporation of Cu and Zn in the catalysts, we tested whether the presence of these two components influenced the performance of the catalyst. The $NiMgCuO_x$ (Zn-free) and $NiMgZnO_x$ (Cu-free) catalysts were synthesized with the same procedure as $NiMgCuZnO_x$, but without inclusion of the $CuCl_2$ and $ZnCl_2$ precursors, and tested for DRM. Compared to $NiMgCuZnO_x$, the catalyst without Zn deactivates faster (Figure 2A and 2B). Thus, the inclusion of Zn in the catalyst was indispensable for stable performance. XRD patterns of spent samples revealed that $NiMgCuO_x$ shows more significant secondary metallic phases after 70 h DRM compared to spent $NiMgCuZnO_x$ after 120 h DRM, indicating a more stable crystal structure for the catalyst with Zn (Figure S2). In addition, spent $NiMgCuO_x$ shows more significant diffraction peaks corresponding to graphitic carbon compared to spent $NiMgCuZnO_x$. To understand the basicity of the surface, we performed temperature-programmed desorption of CO_2 (CO_2-TPD, Figure S2C). The $NiMgCuZnO_x$ and $NiMgCuO_x$ (Zn-free) catalysts presented weak basic sites with CO_2 desorption peak at 105-135 °C. However, NiMgCuOx (Zn-free) also presented strong basic sites, corresponding to CO_2 desorption above 800 °C. Strong CO_2 adsorption can favor oxidation of deposited carbon through the reverse Boudouard reaction. In fact, $NiMgCuO_x$ (Zn-free) showed enhanced CO_2 dissociation to CO (Figure S2C) during TPD. This evidence suggests that the superior stability of the $NiMgCuZnO_x$ catalyst does not necessarily rely on oxidation of coke, but rather on its ability to physically repel coke off the surface, as explained in following sections. For the Cu-free sample, it reaches peak activity immediately after exposure to the reactant gas flow as shown in Figure S3A and S3B, indicating a much quicker evolution process compared to Cu-loaded samples. However, it also exhibits a rapid loss of activity potentially due to consistent sintering or coke deposition. The removal of Ni resulted in an inert sample without activity for DRM (Figure S3). In summary, the Ni species are indispensable species for the activation of reactants as demonstrated in previous work. [10, 13-17 20] More importantly, Cu and Zn contribute to the formation of a long-term stable structure for DRM.

The induction period observed during DRM over $NiMgCuZnO_x$ suggests that the catalyst reconstructs into a structure that favors the conversion of CH_4 and CO_2. To understand the catalyst reconstruction process, the reaction was conducted with diluted reactants (5% CH_4, 5% CO_2) to extend the induction period (Figure 2C) and study intermediate stages of catalyst reconstruction. For the $NiMgCuZnO_x$ catalyst, CH_4 conversion increases from 0% to 45% in the first 40 h, followed by a slower increase to 56% after 140 h. CO_2 conversion follows the same trend (Figure S4) and the final H_2 to CO ratio reaches 0.8 (Figure 2E). Removing Zn from the catalyst ($NiMgCuO_x$) led to lower conversions and catalyst deactivation, as it was observed when concentrated reactants were used. From this point on, characterization is performed on spent catalyst samples obtained after DRM at 800 °C using a 5/5/90 CH_4/CO_2/Ar mixture.

Raman spectra were measured on spent samples to characterize possible coke deposition. Graphite-type coke accumulated on the surface after 15 and 140 h of TOS (Figure S5). Temperature-programmed oxidation (TPO) experiments were performed to quantify coke deposition with TOS (Figure 2F). Notably, the coke content reached significant levels: 9 wt% after 15 h of TOS and 17 wt% at 50 h of TOS; such a deposition could fully cover the surface of the catalyst if uniformly distributed. However, despite this, the conversion of reactants consistently increased with TOS (Figure 2D and Figure S4), raising questions about coke blocking the active sites. Visual inspection of the reactor after conducting DRM showed accumulation of coke in the quartz wool used to hold the catalyst bed in place (Figure S5), which led us to hypothesize that coke would detach from the catalyst surface during DRM. To test this hypothesis, the spent catalysts

were separated from the quartz sand and quartz wool used during DRM. TPO characterization was performed on the separated catalyst, using fresh quartz wool to hold the catalyst bed in place. TPO results showed that the separated catalyst presented some coke deposition, in agreement with Raman spectroscopy results. However, the separated catalyst exhibited a coke weight percentage of only 1.16 wt% after 20 h of TOS, decreasing to 0.17 wt% after 140 h of TOS. This evidence confirmed that the catalyst itself does not further accumulate carbon on the surface as the reaction proceeds. Rather, the majority of coke is repelled from the catalyst and it accumulates in the quartz wool and sand. Even when the reactant feed was 50% CH_4 and 50% CO_2, the coke content measured by TPO remained low, at just 0.86 wt% after 110 h of TOS. The minimal coke deposition on $NiMgCuZnO_x$ significantly contributes to its stability observed during long-term DRM tests.

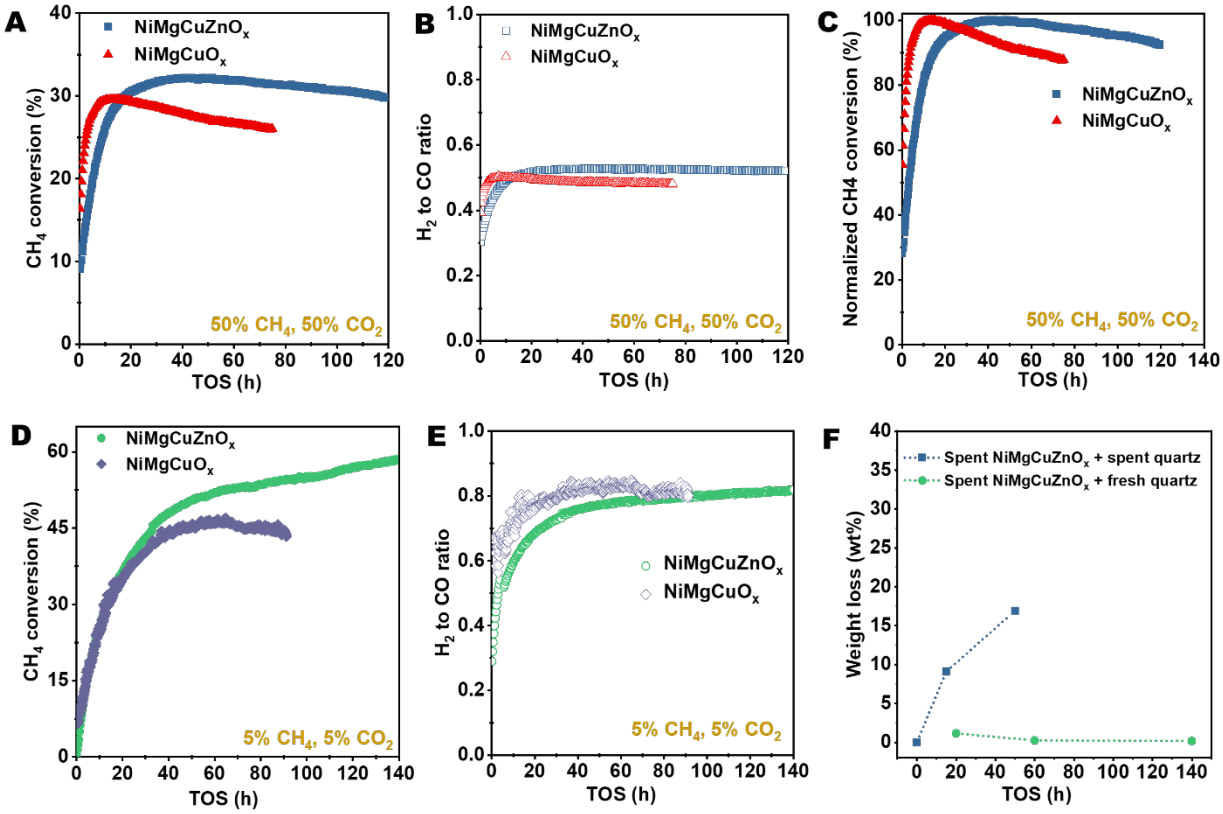

Figure 2. DRM performance and resistance to coke evaluation.
(A) CH_4 conversion over NiMgCuZnOx and NiMgCuOx using concentrated feed (50% CH_4, 50% CO_2, $WHSV_{reactants}$ = 320 L g_{cat}^{-1} h^{-1}).

(B) H_2/CO ratio over $NiMgCuZnO_x$ and $NiMgCuO_x$ using concentrated feed.

(C) Normalized CH_4 conversion over $NiMgCuZnO_x$ and $NiMgCuO_x$ using concentrated feed.

(D) CH_4 conversion over $NiMgCuZnO_x$ and $NiMgCuO_x$ using a diluted feed (5% CH_4, 5 % CO_2, balance Ar, $WHSV_{reactants}$ = 32 L g_{cat}^{-1} h^{-1}).

(E) H_2/CO ratio over $NiMgCuZnO_x$ and $NiMgCuO_x$ using a diluted feed.

(F) Coke deposition measured by TPO on spent $NiMgCuZnO_x$ + spent quartz (quartz sand and quartz wool) and spent $NiMgCuZnO_x$ + fresh quartz.

Structural and electronic evolution of $NiMgCuZnO_x$ under reducing and DRM conditions

To study the thermal stability of the $NiMgCuZnO_x$ catalyst under reducing conditions, in situ XRD and near-ambient pressure X-ray photoelectron spectroscopy (NAP-XPS) characterization were performed. As shown in Figure 3A, the sample preserves the main diffraction peaks corresponding to the rock salt crystal structure throughout the temperature ramping process in H_2. Meanwhile, two small diffraction peaks located at 43.6 and 50.8° emerge over 800 °C, which are attributed to the formation of $Cu_{0.81}Ni_{0.19}$ alloy nanoparticles. In the Ni 2p NAP-XPS spectra (Figure 3B), the characteristic peak of Ni^{2+} located at 854.93 eV decreases as the temperature is increased from 25 to 760 °C, accompanied by the increase of the peak at 851.53 eV corresponding to metallic Ni species.[36, 37] At 760 °C, a fraction of surface Ni species preserve their oxidized valence as indicated by the broad peak 854.89 eV. In comparison, the feature peak for Cu species exhibits consistent shift from 933.94 to 931.33 eV, suggesting the progressive reduction of Cu^{2+} to Cu^0 (Figure 3C).[38, 39] At 760 °C, nearly all the surface Cu species are reduced to the metallic form as no Cu^{2+} feature peak was observed (Figure 3D). In summary, in situ XRD and NAP-XPS analysis confirm the reduction of both Ni^{2+} and Cu^{2+} species in the $NiMgCuZnO_x$ catalyst to their metallic forms during pretreatment in H_2 at high temperature. Compared with Cu^{2+}, the Ni^{2+} species exhibit a considerably slower reduction process followed by alloy formation with Cu, accounting for the observed induction period during DRM catalysis.

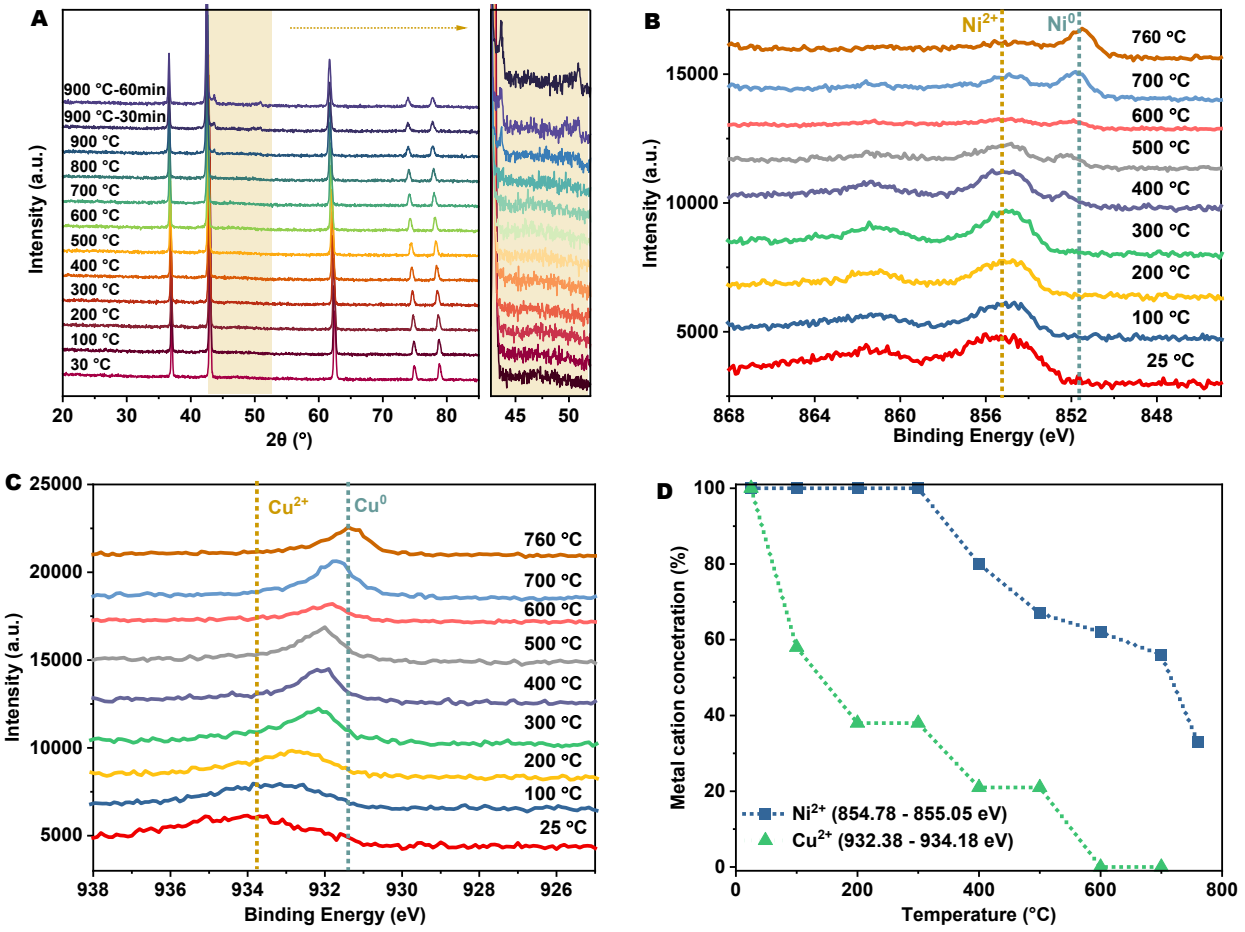

Figure 3. Exsolution behavior of metal oxide solid solution under reducing condition.
(A) In situ XRD patterns of $NiMgCuZnO_x$ recorded during reduction in 2% H_2/N_2 atmosphere and heating from 30 to 900 °C.

(B) Ni 2p3/2 spectra of $NiMgCuZnO_x$ collected under 1 mbar H_2 and heating from 25 to 760 °C.

(C) Cu 2p3/2 NAP-XPS spectra of $NiMgCuZnO_x$ collected under 1 mbar H_2 and heating from 25 to 760 °C.

(D) Concentration of Ni^{2+} and Cu^{2+} as function of temperature during NAP-XPS characterization.

Next, we investigated the evolution of the crystal structure and surface composition as the DRM reaction proceeds. XRD patterns were measured on reduced and spent (generated after DRM in 5% CH_4/5% CO_2) $NiMgCuZnO_x$ samples to characterize changes in their crystalline structure. As illustrated in Figure 4A, diffraction peaks, located at 44.4°, 51.8°, and 76.1°, emerged after reduction, confirming that ex situ XRD can resemble the changes in crystal structure observed via in situ XRD under a reducing atmosphere. The intensities of these diffraction peaks increased with TOS under DRM. Slight differences between the position of these peaks when performing in situ or ex situ XRD may be due to different H_2 concentrations and exposure time. These peaks lay in-between those of metallic Ni and metallic Cu (Figure S6),[40] supporting the formation of bimetallic nanoparticles. According to bimetallic references, these new peaks in the reduced samples are positioned between the compositions of $Cu_{0.14}Ni_{0.86}$ (00-066-0204) and $Cu_{0.5}Ni_{0.5}$ (03-065-7246), as detailed in Figure S6A-S6C. Interpolation of the diffraction peaks suggests a bimetallic composition of ~80% Ni and ~20% Cu (Ni:Cu =4), which agrees with surface sensitive X-ray photoelectron spectroscopy (XPS) results, as shown below (Figure 5A). To confirm that the NiCu alloy exists under reaction conditions, in situ XRD was performed at 800 °C under 0.5% CO_2/0.5%CH_4/He. Indeed, the NiCu alloy is stable under DRM conditions, although the exact 2θ value (NiCu alloy compositions) may be influenced by the reactant concentration and flow conditions during the experiment (Figure S6D).

Besides, X-ray pair distribution function (PDF) characterization of the reduced and spent $NiMgCuZnO_x$ shows different peaks compared to the as-synthesized one, also suggesting the potential formation of an alloy phase (Figure S7). HAADF-STEM images were obtained to characterize the surface of the $NiMgCuZnO_x$ catalyst. Post-reduction, the surface of $NiMgCuZnO_x$ exhibited significant reconstruction where NPs (average particle size around 14 nm (Figure 4B and Figure S8A) started to form on the surface. Elemental mapping revealed that the exsoluted nanoparticles were NiCu alloy, as suggested by XRD, whereas Mg remained dispersed (Figure 4B). With extended TOS of 15 and 80 h, the mean particle size grew to 17 nm and 28 nm, respectively (Figure 4B-4D and Figure S8B-S8C). Elemental mapping of the 80 h spent sample (Figure 4D) showed clear overlap of Ni and Cu on the exsolved nanoparticles, which supports the formation of bimetallic NPs.

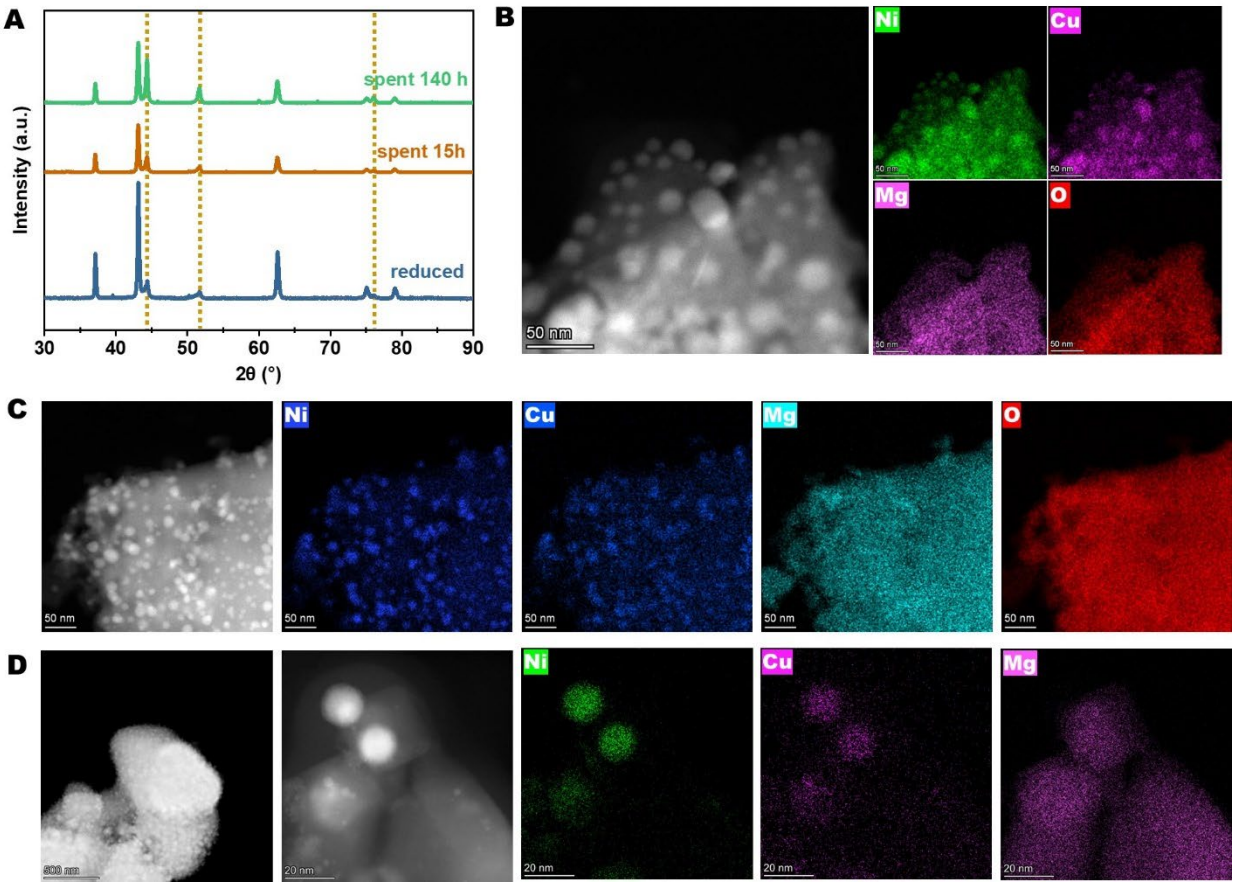

Figure 4. Characterization of reduced and spent catalysts.
(A) XRD patterns of reduced, spent NiMgCuZnOx after 15 h and 140 h DRM.

(B) HAADF-STEM images and elemental mapping of reduced $NiMgCuZnO_x$ catalyst.

(C) HAADF-STEM images and elemental mapping of spent NiMgCuZnOx catalyst after TOS of 15 h.

(D) HAADF-STEM images and elemental mapping of spent NiMgCuZnOx catalyst after TOS of 80 h.

To elucidate the chemical properties of the reconstructed catalyst, a combination of spectroscopic techniques was employed. Diffuse reflectance infrared Fourier transform spectroscopy (DRIFTS) of CO adsorption (Figure S9) showed a vibrational mode at 2117 cm^{-1} for the as-synthesized $NiMgCuZnO_x$ catalyst, which showed up at 2048 cm^{-1} upon reductive treatment. Adsorption bands were undistinguishable when the spent catalyst sample (after 80 h TOS) was exposed to CO, which could be due to darkening of the sample and/or less accessible surface sites (Figure S9). However, the comparison between the CO adsorption spectrum (in the presence of gaseous CO) on the spent $NiMgCuZnO_x$ and gas-phase CO reference (Figure S10) suggested some interaction of CO with surface sites with a slight enhancement of the vibrational mode around 2173 cm^{-1}. Next, we used ex situ XPS to study the near-surface electronic environment of the metal sites and the elemental composition near the surface. Like NAP-XPS, ex situ XPS results showed the reduction of Ni^{2+} and Cu^{2+} during pretreatment and DRM as characteristic peaks of Cu^{1+} and Ni^{1+} emerged at 933.0 and 853.1eV, respectively (Figure S11). Meanwhile, the surface composition also changed significantly. As shown in Figure 5A, the as-synthesized $NiMgCuZnO_x$ catalyst had a Ni-rich surface with identical Mg and Cu contents. After reduction, the concentration of Ni and Cu at the surface decreased, whereas the concentration of Mg increased. Once the DRM reaction was conducted over the $NiMgCuZnO_x$ catalyst, the concentration of Ni further decreased, the concentration of Mg further increased, but the concentration of Cu remained constant compared to the concentration obtained after H_2 pretreatment. With extended TOS, the concentration of Ni and Mg fluctuated slightly and the concentration of Cu remained constant. The Ni:Cu ratio at the near-surface during DRM was between 4 and 5, showing excellent agreement with our estimation via XRD (Figure S6). Further analysis with low-energy ion scattering (LEIS) confirmed the change of surface elements at the topmost layer (around 0.5 nm depth) of the catalyst (Figure 5B and Figure S12). Clearly, Mg was enriched at the surface on the spent catalysts, whereas Ni, Cu and Zn were depleted. Enrichment of Mg at the surface rises the question of whether strong metal-suport interactions (SMSI) are present and a MgO_x overlayer has climbed over the NiCu nanoparticles. Elemental mapping of the spent catalysts showed no evident coverage by MgO_x (Figure S13); instead, TEM images showed overlayers of carbon covering the catalyst surface (Figure S14). This graphitic carbon (as shown via Raman, Figure S5) has a lattice spacing of 3.53 Å, which deviates from the typical value of 3.35 Å.[41] However, increased lattice spacing for graphitic carbon was reported before.[42, 43] Based on this evidence, we proposed that the top surface of the $NiMgCuZnO_x$ catalyst became enriched with carbon-covered NiCu nanoparticles, and that the surface of the solid solution support near the exsoluted NiCu nanoparticles is thus enriched with Mg. During DRM, the surface accumulates some carbon deposits which were constantly removed to free the active sites (Figure 1A). Inductively coupled plasma atomic emission spectroscopy (ICP-AES) was performed to evaluate the bulk concentration of metals in the as-synthesized, pretreated and spent $NiMgCuZnO_x$ sample (Table S1). ICP-AES analysis revealed non-identical metal loadings (oxygen-free basis) in the as-synthesized $NiMgCuZnO_x$ sample: Ni (31.3 mol%) and Mg (49.0 mol%) are the predominant components, followed by minor Cu (18.5 mol%) and a trace amount of Zn (1.21 mol%). The significantly lower concentration of Zn could be attributed to the relatively higher volatility of Zn. Fracchia et al.[44] have explored the role of entropy in the formation and stabilization of the high-entropy oxide $Ni_{0.2}Mg_{0.2}Co_{0.2}Cu_{0.2}Zn_{0.2}O$ with a rock salt structure. It was demonstrated that a homogenous rock salt crystal phase can be formed with two, three or four components as long as the Cu and Zn loading are lower than 20 mol% (oxygen-free basis), which is the case in our catalyst. After pretreatment (O_2 900 °C, H_2 800 °C), there was some fluctuation in the relative concentrations, likely due to volatility at high temperatures. In particular, upon pretreatment, the concentration of Zn (oxygen-free basis) decreased to 0.12 mol%, and further down to 0.01 % after performing DRM with concentrated reactants for 30 h. As showed in Figure 2A, the $NiMgCuZnO_x$ catalyst was stable past 30 h TOS, which suggested that the presence of Zn in the initial structure promotes a stable catalyst despite Zn vaporizing under the harsh DRM reaction conditions.

To elucidate the evolution of the bonding and electronic environment of the metal species, ex situ XAS spectra were collected to characterize the valence and local coordination environment of Ni and Cu. Figure 5C shows that in the as-synthesized sample, the Ni species predominantly existed as Ni^{2+} as indicated by the overlapping absorption edge and characteristic pre-edge peak at 8330.4 eV, corresponding to the dipole-forbidden 1s → 3d transition.[45] The $NiMgCuZnO_x$ exhibited a distinctive white-line peak and k-space

oscillations (Figure S15), suggesting a unique coordination environment. Despite the complexity of the solid solution structure and bimetallic interactions which preclude a complete resolution of the second-shell atoms surrounding the Ni atoms, the data compellingly highlighted the structural differences between the as-synthesized $NiMgCuZnO_x$ and monometallic oxide references. Different from the NiO reference, in as-synthesized $NiMgCuZnO_x$ Ni^{2+} had a coordination number (CN) of 2.7 for the first-shell coordinated O and CN of 3.1 for the second-shell Ni-Ni bonding (Table S2). The analysis of R-space EXAFS (Figure 5D and Figure S16) and corresponding fitting results strongly indicated the formation of components containing heterometallic bonds, rather than a mere mixture of individual oxides. After reduction, only a minor portion of Ni^{2+} was reduced, as evidenced by a slight shift in the absorption edge. During DRM, a greater fraction of Ni^{2+} was reduced to the metallic form, with the edge energy shifting closer to that of the Ni foil reference. After 150 h of TOS, only a small fraction of Ni sites remained in an oxidized state, indicated by the persistent white-line peak. None of the XANES spectra can be adequately described by a linear combination of NiO and metallic Ni, further supporting the presence of a complex mixture of species including oxides, metals, and bimetallic alloys.

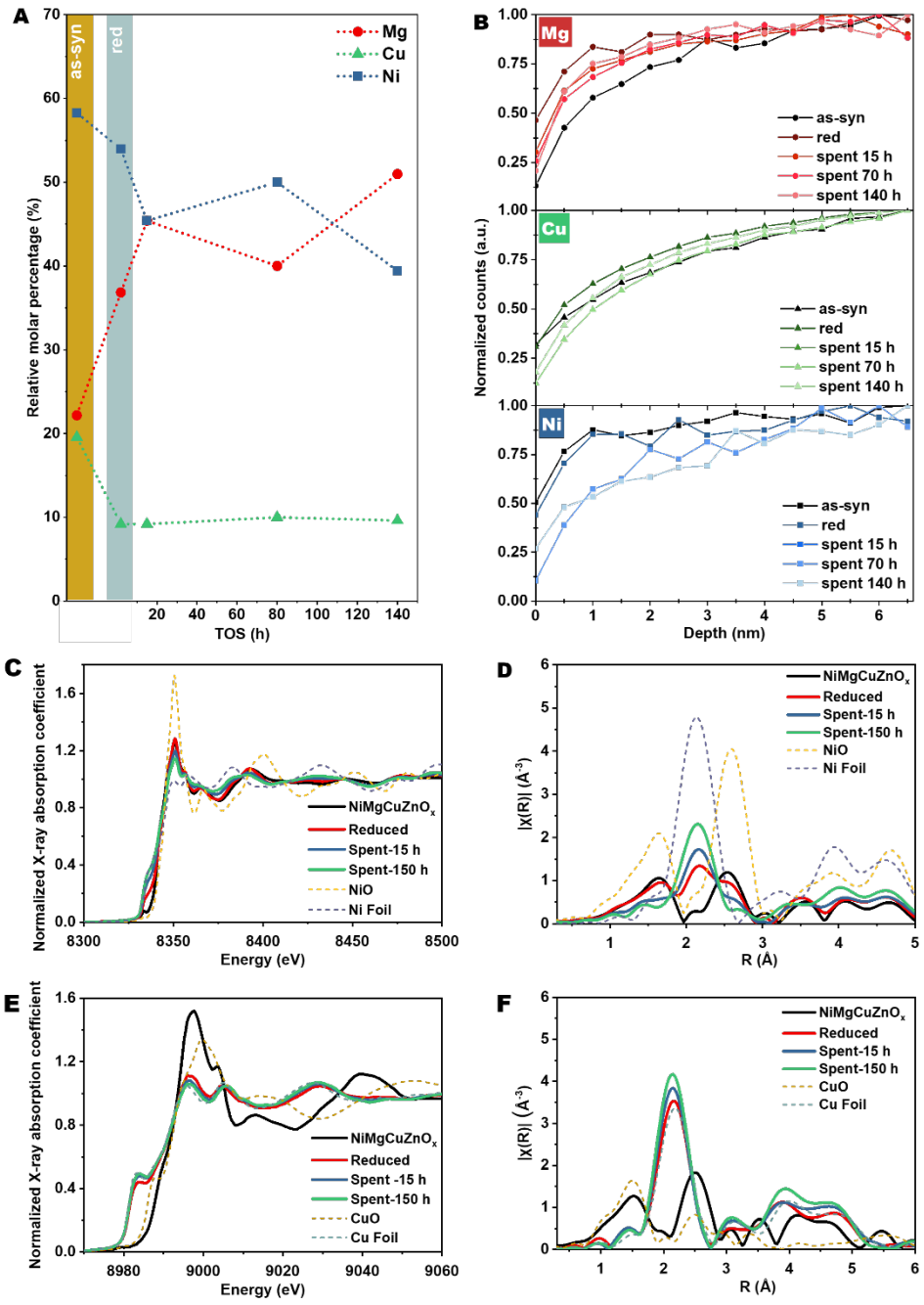

Figure 5. Structural and valence variation of spent catalysts from DRM.
(A) Surface composition of NiMgCuZnOx characterized by ex situ XPS.

(B) LEIS elemental profiles of NiMgCuZnOx sample at different stages of catalytic performance measurement. “spent X h” refers to a spent catalyst during DRM at 800 °C for X h.

(C) Ni K edge XANES spectra of as-synthesized, reduced and spent samples with NiO and Ni foil reference. “red” refers to calcination at 900 °C followed by reduction at 800 °C. “spent X h” refers to a spent catalyst during DRM at 800 °C for X h.

(D) Ni K edge R-space EXAFS spectra.

(E) Cu K edge XANES spectra of as-synthesized, reduced and spent samples with CuO and Cu foil reference.

(F) Cu K edge R-space EXAFS spectra.

On the other hand, the dominant Cu species in the as-synthesized sample were Cu^{2+}, but the shape of white-line peak was distinctive from the oxide references (Figure 5E). In contrast to Ni, most of the Cu^{2+} species were reduced to metallic form during the reduction step and were completely reduced after 15 h of DRM. This rapid transformation matches the constant near-surface Cu concentration observed for the reduced and spent catalyst samples (Figure 5A). Given the higher concentration of Ni in the bulk phase and its slower reduction, the formation of a bimetallic phase was more discernible in the XAS spectra of Cu. EXAFS fitting of the Cu K-edge indicated a first-shell Cu-Cu coordination number of 10.7 in the metallic phase, yet the bonding distance was shorter than that observed in the Cu foil reference (Figure 5F, Table S3). Considering the shorter bonding distance of Ni-Ni in metallic Ni phase, this reduced bond distance could be attributed to the formation of a Cu-Ni bimetallic alloy, due to the higher content of Ni relative to Cu. Such minimal changes could be obscured by the high Ni content in the XAS analysis of Ni. Furthermore, the k-space EXAFS of Cu also demonstrated shifts in oscillation at long-range distances, further suggesting the formation of a bimetallic phase (Figure S17). Collectively, these characterization results suggested that most Cu^{2+} species underwent exsolution to the surface, forming metallic nanoparticles during pretreatment, while this process was considerably slower for Ni^{2+}. The gradually reduced Ni^{2+} species then formed bimetallic nanoparticles on the oxide solution support, thereby enhancing reactant conversion.

Because the exsolved NiCu nanoparticles were suggested as the primary active phase for methane reforming, the observed increase in reactant conversion (Figure 2A) may result from either the evolution of NiCu species with enhanced reactivity as the reaction process, or an increased density of the active sites with TOS. To investigate these possibilities, temperature-programmed surface reaction (TPSR) was conducted on catalyst samples recovered after 16 and 80 h of TOS during DRM (Figure S18). We recorded the mass spectrometer signal as a function of temperature during a 10 $°C \cdot min^{-1}$ ramp, with the purpose of comparing the onset temperature for DRM of both samples. The onset temperature for CH_4 conversion during the TPSR experiment was almost identical for the recovered catalyst samples, suggesting that the reactivity of the surface sites on both samples was similar and that the enhanced conversion as TOS increased may be attributed to a higher density of active sites. The dynamic exsolution of NiCu bimetallic nanoparticles with TOS, concurrent with their moderate particle growth, renders the estimation of net active site density challenging.

To test the mobility of the carbon deposits, we performed chemical looping experimentation during 20 h, for a total of 21 cycles (Figure S19 and Figure 6). After pretreating the catalyst in O_2 at 900 °C and H_2 at 800 °C, the catalyst was kept at 800 °C. The catalyst bed was flushed with Ar, followed by exposure to 5% CH_4/Ar, flush with Ar, and a flow of 5% CO_2/Ar. This sequence constitutes a cycle of chemical looping. During the first cycle, CH_4 first decomposed into H_2 and surface carbon, upon exposure to CO_2, CO was produced. This evidence suggested that the carbon left in the surface upon CH_4 decomposition can be oxidized by CO_2 in a decoupled step through the reverse Boudouard reaction. In later cycles, CO was also produced during the CH_4 flow step, suggesting that the surface is enriched with active oxygen that evolves as CO. Similarly, H_2 was produced during CO_2 flow of the surface, suggesting that hydrogenated species were left on the surface after CH_4 flush, and evolve as H_2. During the chemical looping experiment, H_2 to CO ratio increased with TOS as it happened during the constant flow experiment (Figure S18 and Figure 2C).

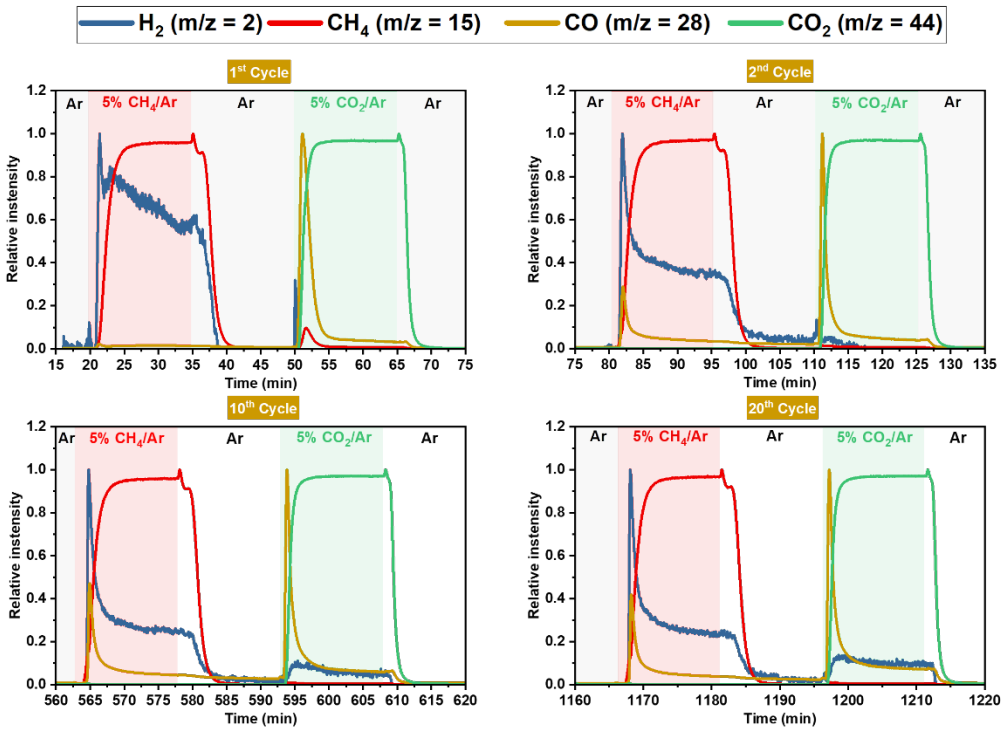

Figure 6. Study DRM chemical looping. Normalized intensities of select cycles during DRM Chemical looping at 800 °C. NiMgCuZnO$_x$ catalyst was pretreated in O2 at 900 °C and H_2 at 800 °C.

CONCLUSIONS

To address the persistent challenge of catalyst deactivation in DRM, we rationally designed a multimetallic solid-solution metal oxide catalyst that delivers both stability and flexibility under harsh operating conditions. The as-synthesized NiMgCuZnO$_x$ solid solution exhibited homogeneous metal distribution and greater resistance to reduction compared to the individual monometallic oxides of Ni and Cu, ensuring structural integrity before reaction. Upon reductive pretreatment at 800 °C and subsequent DRM operation, the catalyst reconstructs to exsolve tightly anchored Ni–Cu nanoparticles that act as robust active sites. Unlike conventional Ni-based catalysts that suffer from sintering and coking, the exsolved NPs remain well-dispersed, while the weakened coke–surface interactions enable continuous detachment of carbon, suppressing deactivation. XAS and NAP-XPS confirmed that Ni^{2+} reduction proceeds more slowly than Cu^{2+}, leading to progressive Ni enrichment of the bimetallic NPs during DRM operation. Complementary TPSR studies indicated that the intrinsic activity of the Ni–Cu sites remains constant over time on stream, with enhanced conversion arising from the dynamic generation of additional active sites. This solid-solution approach directly addresses the high-temperature instability that has long limited DRM by coupling controlled NPs exsolution with self-regeneration of active sites, providing a pathway toward durable and scalable catalysts for industrial syngas production from methane and CO_2.

ACKNOWLEDGMENTS

This research was sponsored by the U.S. Department of Energy (DOE), Office of Science, Office of Basic Energy Sciences, Chemical Sciences, Geosciences, and Biosciences Division, Catalysis Science program. Part of the research were carried out at National Synchrotron Light Source II (NIST beamline 6-BM), a U.S.

DOE Office of Science User Facility operated for the DOE Office of Science by Brookhaven National Laboratory under Contract No. DE-SC0012704. Part of the research was performed on APS beam time award: https://doi.org/10.46936/APS-188511/60013158, from the Advanced Photon Source, a U.S. DOE Office of Science User Facility operated for the DOE Office of Science by Argonne National Laboratory under Contract No. DE-AC02-06CH11357. Some of the work including Raman spectra measurement was conducted as part of a user project at the Center for Nanophase Materials Science (CNMS), which is a U.S. DOE Office of Science User Facility located at Oak Ridge National Laboratory. We thank Dr. Ryan Thorpe (Lehigh University Institute for Functional Materials and Devices) for performing LEIS analysis.

AUTHOR CONTRIBUTIONS

θ These authors contributed equally
*Corresponding authors: yangz3@ornl.gov (Z.Y.); pologarzonf@ornl.gov (F.P.), dais@ornl.gov (S.D.)

DECLARATION OF INTERESTS

The authors declare no competing interests.

SUPPLEMENTAL INFORMATION

Figures S1–S19, and Tables S1–S3.
Microscopy, XRD, CO_2 TPD, DRM catalytic performance, Raman spectroscopy, X-ray PDF, particle size distribution, CO DRIFTS, XPS, LEIS, XAS, TPSR, DRM chemical looping, ICP results, EXAFS fitting results.

REFERENCES

(1) Bruijnincx, P. C.; Weckhuysen, B. M. Shale gas revolution: an opportunity for the production of biobased chemicals? *Angew. Chem. Int. Ed.* **2013**, *46* (52), 11980-11987.
(2) Zhang, H.; Sun, Z.; Hu, Y. H. Steam reforming of methane: Current states of catalyst design and process upgrading. *Renew. Sustain. Energy Rev.* **2021**, *149*, 111330.
(3) García, L. Hydrogen production by steam reforming of natural gas and other nonrenewable feedstocks. In *Compendium of hydrogen energy*, Elsevier, 2015; pp 83-107.
(4) Zhu, Q.; Zhou, H.; Wang, L.; Wang, L.; Wang, C.; Wang, H.; Fang, W.; He, M.; Wu, Q.; Xiao, F.-S. Enhanced CO_2 utilization in dry reforming of methane achieved through nickel-mediated hydrogen spillover in zeolite crystals. *Nat. Catal.* **2022**, *5* (11), 1030-1037. DOI: 10.1038/s41929-022-00870-8.
(5) Song, Y.; Ozdemir, E.; Ramesh, S.; Adishev, A.; Subramanian, S.; Harale, A.; Albuali, M.; Fadhel, B. A.; Jamal, A.; Moon, D.; et al. Dry reforming of methane by stable Ni–Mo nanocatalysts on single-crystalline MgO. *Science* **2020**, *367* (6479), 777-781. DOI: doi:10.1126/science.aav2412.
(6) Pakhare, D.; Spivey, J. A review of dry (CO2) reforming of methane over noble metal catalysts. *Chem Soc Rev* **2014**, *43* (22), 7813-7837, 10.1039/C3CS60395D. DOI: 10.1039/C3CS60395D.
(7) Akri, M.; Zhao, S.; Li, X.; Zang, K.; Lee, A. F.; Isaacs, M. A.; Xi, W.; Gangarajula, Y.; Luo, J.; Ren, Y.; et al. Atomically dispersed nickel as coke-resistant active sites for methane dry reforming. *Nat. Commun.* **2019**, *10* (1), 5181. DOI: 10.1038/s41467-019-12843-w.
(8) Ruckenstein, E.; Hu, Y. H. Carbon dioxide reforming of methane over nickel/alkaline earth metal oxide catalysts. *Applied Catalysis A: General* **1995**, *133* (1), 149-161. DOI: https://doi.org/10.1016/0926-860X(95)00201-4.
(9) Bradford, M.; Vannice, M. CO_2 reforming of CH_4. *Catal. Rev.* **1999**, *41* (1), 1-42.
(10) Al-Fatesh, A. S.; Patel, N.; Fakeeha, A. H.; Alotibi, M. F.; Alreshaidan, S. B.; Kumar, R. Reforming of methane: Effects of active metals, supports, and promoters. *Catal. Rev.* **2023**, 1-99.
(11) Velty, A.; Corma, A. Advanced zeolite and ordered mesoporous silica-based catalysts for the conversion of CO 2 to chemicals and fuels. *Chemical Society Reviews* **2023**, *52* (5), 1773-1946.
(12) Kim, J.-H.; Suh, D. J.; Park, T.-J.; Kim, K.-L. Effect of metal particle size on coking during CO_2 reforming of CH_4 over Ni–alumina aerogel catalysts. *Appl. Catal. A Gen.* **2000**, *197* (2), 191-200.
(13) Ruckenstein, E.; Hu, Y. H. Carbon dioxide reforming of methane over nickel/alkaline earth metal oxide catalysts. *Appl. Catal. A Gen.* **1995**, *133* (1), 149-161.
(14) Jafarbegloo, M.; Tarlani, A.; Mesbah, A. W.; Muzart, J.; Sahebdelfar, S. NiO–MgO solid solution prepared by sol–gel method as precursor for Ni/MgO methane dry reforming catalyst: effect of calcination temperature on catalytic performance. *Catal. Lett.* **2016**, *146*, 238-248.
(15) Ruckenstein, E.; Hu, Y. H. The effect of precursor and preparation conditions of MgO on the CO_2 reforming of CH_4 over NiO/MgO catalysts. *Appl. Catal. A Gen.* **1997**, *154* (1-2), 185-205.
(16) Xu, B.-Q.; Wei, J.-M.; Wang, H.-Y.; Sun, K.-Q.; Zhu, Q.-M. Nano-MgO: novel preparation and application as support of Ni catalyst for CO_2 reforming of methane. *Catal. Today* **2001**, *68* (1-3), 217-225.
(17) Song, Y.; Ozdemir, E.; Ramesh, S.; Adishev, A.; Subramanian, S.; Harale, A.; Albuali, M.; Fadhel, B. A.; Jamal, A.; Moon, D. Dry reforming of methane by stable Ni–Mo nanocatalysts on single-crystalline MgO. *Science* **2020**, *367* (6479), 777-781.
(18) Peng, H.; Zhang, X.; Han, X.; You, X.; Lin, S.; Chen, H.; Liu, W.; Wang, X.; Zhang, N.; Wang, Z.; et al. Catalysts in Coronas: A Surface Spatial Confinement Strategy for High-Performance Catalysts in Methane Dry Reforming. *ACS Catal* **2019**, *9* (10), 9072-9080. DOI: 10.1021/acscatal.9b00968.
(19) Akri, M.; Zhao, S.; Li, X.; Zang, K.; Lee, A. F.; Isaacs, M. A.; Xi, W.; Gangarajula, Y.; Luo, J.; Ren, Y.; et al. Atomically dispersed nickel as coke-resistant active sites for methane dry reforming. *Nat Commun* **2019**, *10* (1), 5181. DOI: 10.1038/s41467-019-12843-w.
(20) He, L.; Li, M.; Li, W.-C.; Xu, W.; Wang, Y.; Wang, Y.-B.; Shen, W.; Lu, A.-H. Robust and Coke-free Ni Catalyst Stabilized by 1–2 nm-Thick Multielement Oxide for Methane Dry Reforming. *ACS Catalysis* **2021**, *11* (20), 12409-12416. DOI: 10.1021/acscatal.1c02995.
(21) Zhang, S.; Gao, Y.; Niu, Q.; Zhang, P. Enhancing coke resistance of Ni-based spinel-type oxides by tuning the configurational entropy. *Journal of Catalysis* **2024**, *440*, 115819. DOI: https://doi.org/10.1016/j.jcat.2024.115819.
(22) Li, W.; Zhao, G.; Zhong, J.; Xie, J. Upgrading renewable biogas into syngas via bi-reforming over high-entropy spinel-type catalysts derived from layered double hydroxides. *Fuel* **2024**, *358*, 130155. DOI: https://doi.org/10.1016/j.fuel.2023.130155.
(23) Wu, Z.; Li, M.; Howe, J.; Meyer, H. M.; Overbury, S. H. Probing defect sites on CeO_2 nanocrystals with well-defined surface planes by Raman spectroscopy and O_2 adsorption. *Langmuir* **2010**, *26* (21), 16595-16606. DOI: 10.1021/la101723w.
(24) Ravel, B.; Newville, M. ATHENA, ARTEMIS, HEPHAESTUS: data analysis for X-ray absorption spectroscopy using IFEFFIT. *J. Synchrotron Radiat.* **2005**, *12* (4), 537-541.
(25) Toby, B. H.; Von Dreele, R. B. GSAS-II: the genesis of a modern open-source all purpose crystallography software package. *J. Appl. Crystallogr.* **2013**, *46* (2), 544-549.

(26) Juhás, P.; Davis, T.; Farrow, C. L.; Billinge, S. J. PDFgetX3: a rapid and highly automatable program for processing powder diffraction data into total scattering pair distribution functions. *J. Appl. Crystallogr.* **2013**, *46* (2), 560-566.
(27) Chupas, P. J.; Qiu, X.; Hanson, J. C.; Lee, P. L.; Grey, C. P.; Billinge, S. J. Rapid-acquisition pair distribution function (RA-PDF) analysis. *J. Appl. Crystallogr.* **2003**, *36* (6), 1342-1347.
(28) Han, K.; Wang, S.; Liu, Q.; Wang, F. Optimizing the Ni/Cu ratio in Ni–Cu nanoparticle catalysts for methane dry reforming. *ACS Appl. Nano Mater.* **2021**, *4* (5), 5340-5348.
(29) Song, K.; Lu, M.; Xu, S.; Chen, C.; Zhan, Y.; Li, D.; Au, C.; Jiang, L.; Tomishige, K. Effect of alloy composition on catalytic performance and coke-resistance property of Ni-Cu/Mg (Al) O catalysts for dry reforming of methane. *Appl. Catal. B Environ.* **2018**, *239*, 324-333.
(30) Chatla, A.; Ghouri, M. M.; El Hassan, O. W.; Mohamed, N.; Prakash, A. V.; Elbashir, N. O. An experimental and first principles DFT investigation on the effect of Cu addition to Ni/Al_2O_3 catalyst for the dry reforming of methane. *Appl. Catal. A Gen.* **2020**, *602*, 117699.
(31) Omran, A.; Yoon, S. H.; Khan, M.; Ghouri, M.; Chatla, A.; Elbashir, N. Mechanistic insights for dry reforming of methane on Cu/Ni bimetallic catalysts: DFT-assisted microkinetic analysis for coke resistance. *Catalysts* **2020**, *10* (9), 1043.
(32) Chen, S.; Zaffran, J.; Yang, B. Descriptor design in the computational screening of Ni-based catalysts with balanced activity and stability for dry reforming of methane reaction. *ACS Catal.* **2020**, *10* (5), 3074-3083.
(33) Yu, Y.-X.; Yang, J.; Zhu, K.-K.; Sui, Z.-J.; Chen, D.; Zhu, Y.-A.; Zhou, X.-G. High-throughput screening of alloy catalysts for dry methane reforming. *ACS Catal.* **2021**, *11* (14), 8881-8894.
(34) Chen, H.; Fu, J.; Zhang, P.; Peng, H.; Abney, C. W.; Jie, K.; Liu, X.; Chi, M.; Dai, S. Entropy-stabilized metal oxide solid solutions as CO oxidation catalysts with high-temperature stability. *J Mater Chem A* **2018**, *6* (24), 11129-11133, 10.1039/C8TA01772G. DOI: 10.1039/c8ta01772g.
(35) Chen, H.; Lin, W.; Zhang, Z.; Jie, K.; Mullins, D. R.; Sang, X.; Yang, S.-Z.; Jafta, C. J.; Bridges, C. A.; Hu, X.; et al. Mechanochemical Synthesis of High Entropy Oxide Materials under Ambient Conditions: Dispersion of Catalysts via Entropy Maximization. *ACS Materials Lett* **2019**, *1* (1), 83-88. DOI: 10.1021/acsmaterialslett.9b00064.
(36) Cheng, M.; Fan, H.; Song, Y.; Cui, Y.; Wang, R. Interconnected hierarchical $NiCo_2O_4$ microspheres as high-performance electrode materials for supercapacitors. *Dalton Trans.* **2017**, *46* (28), 9201-9209, 10.1039/C7DT01289F. DOI: 10.1039/C7DT01289F.
(37) Grosvenor, A. P.; Biesinger, M. C.; Smart, R. S. C.; McIntyre, N. S. New interpretations of XPS spectra of nickel metal and oxides. *Surf. Sci.* **2006**, *600* (9), 1771-1779. DOI: https://doi.org/10.1016/j.susc.2006.01.041.
(38) Chen, H.; Lin, W.; Zhang, Z.; Yang, Z.; Jie, K.; Fu, J.; Yang, S.-z.; Dai, S. Facile benzene reduction promoted by a synergistically coupled Cu–Co–Ce ternary mixed oxide. *Chem. Sci.* **2020**, *11* (22), 5766-5771, 10.1039/D0SC02238A. DOI: 10.1039/D0SC02238A.
(39) Tanaka, Y.; Kikuchi, R.; Takeguchi, T.; Eguchi, K. Steam reforming of dimethyl ether over composite catalysts of γ-Al_2O_3 and Cu-based spinel. *Appl. Catal. B Environ.* **2005**, *57* (3), 211-222. DOI: https://doi.org/10.1016/j.apcatb.2004.11.007.
(40) Yang, C.; Xue, W.; Yin, H.; Lu, Z.; Wang, A.; Shen, L.; Jiang, Y. Hydrogenation of 3-nitro-4-methoxy-acetylaniline with H 2 to 3-amino-4-methoxy-acetylaniline catalyzed by bimetallic copper/nickel nanoparticles. *New J. Chem.* **2017**, *41* (9), 3358-3366.
(41) Schäffel, F. The atomic structure of graphene and Its Few-layer counterparts. *Graphene; Elsevier: Amsterdam, The Netherlands* **2013**, *25*, 5-59.
(42) Ruan, C.; Leng, J.; Lian, Y. Electrochemical performance of carbon onions fabricated by electric arc‐discharge method. *Electroanalysis* **2016**, *28* (1), 145-150.
(43) Xu, J.; Zhang, R.; Wang, J.; Ge, S.; Wen, F. Hollow carbon onions with larger lattice spacing obtained by chlorination of the ball-milled SiC. *Mater. Lett.* **2012**, *88*, 168-170.
(44) Fracchia, M.; Coduri, M.; Manzoli, M.; Ghigna, P.; Tamburini, U. A. Is configurational entropy the main stabilizing term in rock-salt Mg0. 2Co0. 2Ni0. 2Cu0. 2Zn0. 2O high entropy oxide? *Nat. Commun.* **2022**, *13* (1), 2977.
(45) Pickering, I. J.; George, G. N.; Lewandowski, J. T.; Jacobson, A. J. Nickel K-edge X-ray absorption fine structure of lithium nickel oxides. *J. Am. Chem. Soc.* **1993**, *115* (10), 4137-4144.

TOC

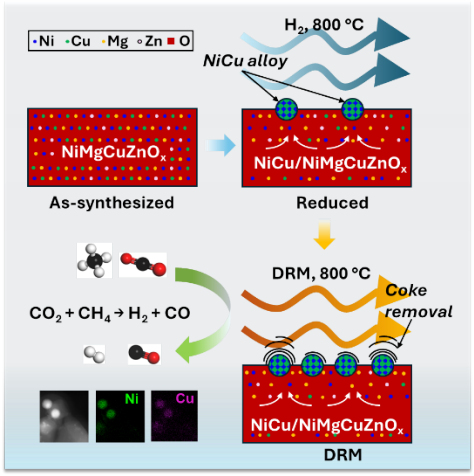
Ni Cu Mg Zn O
H2, 800 °C
NiCu alloy
NiMgCuZnOx
NiCu/NiMgCuZnOx
As-synthesized
Reduced
DRM, 800 °C
Coke removal
CO2 + CH4 → H2 + CO
Ni
Cu
NiCu/NiMgCuZnOx
DRM

Stable Co-valorization of Carbon Dioxide and Methane via Dynamic Reconstruction of a Metal Oxide Solid Solution Catalyst

Junyan Zhang[1, θ], Meijia Li[1, θ], Yuanyuan Li[1], Nabihan B. Abdul Rahman[1], Hailing Yu[2], Kevin Siniard[2], Alexander S. Ivanov[1], Xin Wang[1], Harry M. Meyer III[1], Shize Yang[3], Leighanne C. Gallington[4], Victoria Cooley[4], J. Anibal Boscoboinik,[5] Zili Wu[1, 6], Zhenzhen Yang[1, *], Felipe Polo-Garzon[1, *], and Sheng Dai[1, 2, *]

[1]Chemical Sciences Division, Oak Ridge National Laboratory, Oak Ridge, TN 37831, USA
[2]Department of Chemistry, University of Tennessee Knoxville, Knoxville, TN 37996, USA
[3]Aberration Corrected Electron Microscopy Core, Yale University, New Haven, CT 06516, USA
[4]X-Ray Science Division, Advanced Photon Source, Argonne National Laboratory, Lemont, IL 60439, USA
[5]Center for Functional Nanomaterials, Brookhaven National Laboratory, Upton, New York 11973, USA
[6]Center for Nanophase Materials Sciences, Oak Ridge National Laboratory, Oak Ridge, TN 37831, USA

*Corresponding authors: yangz3@ornl.gov (Z.Y.); pologarzonf@ornl.gov (F.P.), dais@ornl.gov (S.D.)

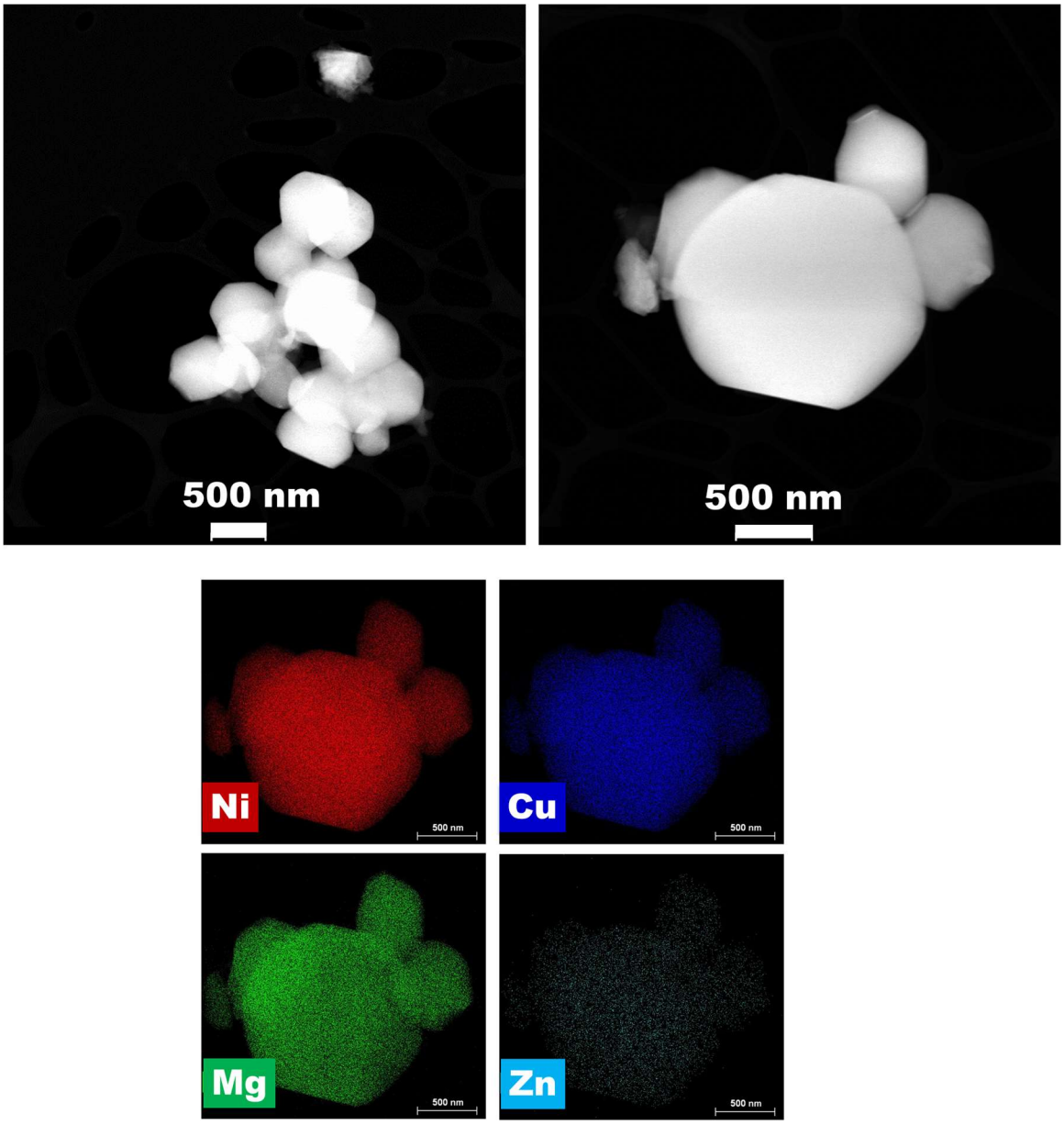

Figure S1. High-angle annular dark-field scanning transmission electron microscopy (HAADF-STEM) images of as-synthesized $NiMgCuZnO_x$ and elemental mapping.

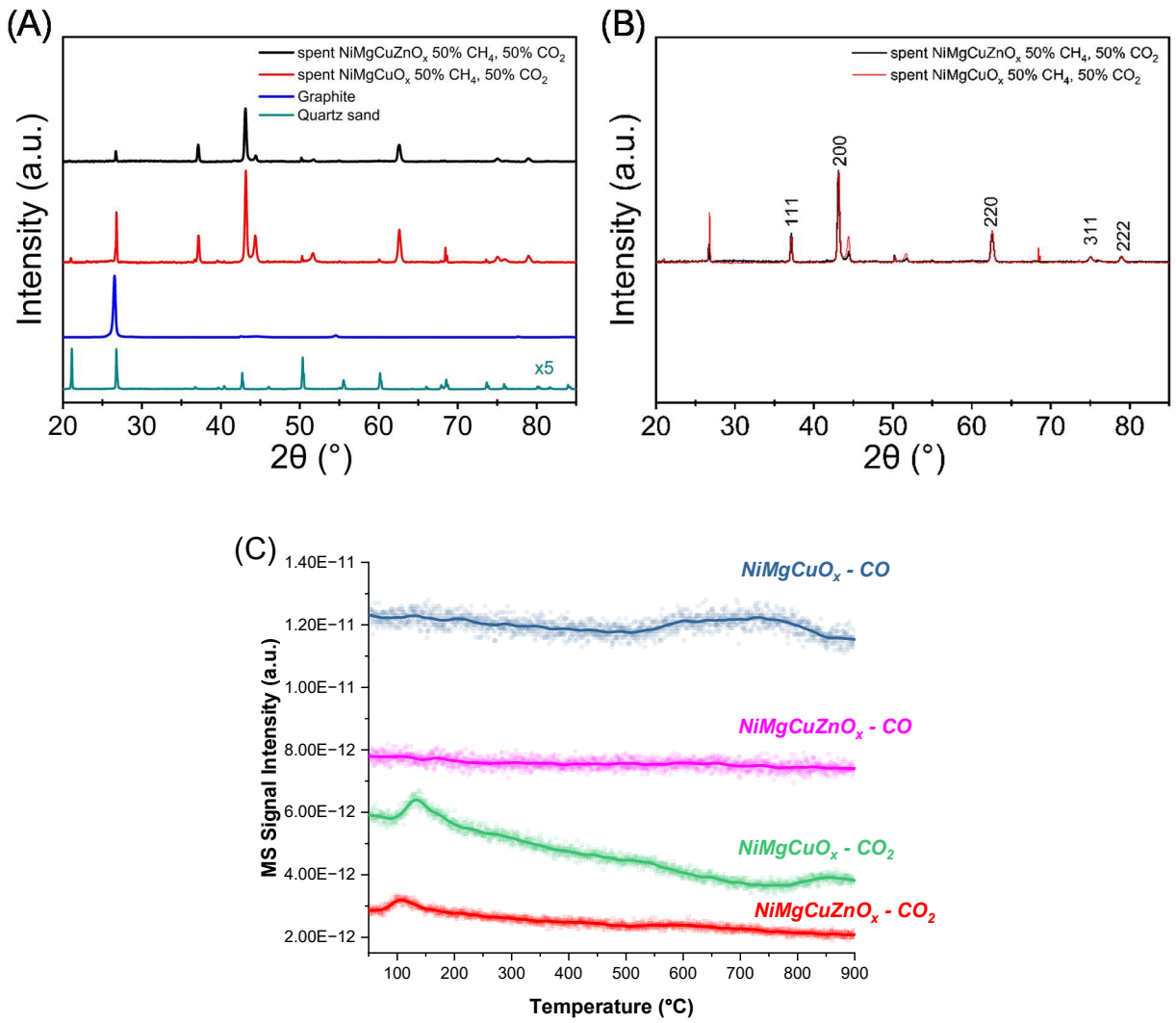

Figure S2. (A) XRD patterns of spent $NiMgCuZnO_x$ and $NiMgCuO_x$ after DRM at 800 °C. The intensity of the diffraction pattern for quartz sand is multiplied by 5 times for comparison. (B) Comparison of diffraction patterns for NiMgCuZnOx and NiMgCuOx catalysts after normalization using (200) diffraction peak. (C) CO_2-TPD of $NiMgCuZnO_x$ and $NiMgCuO_x$.

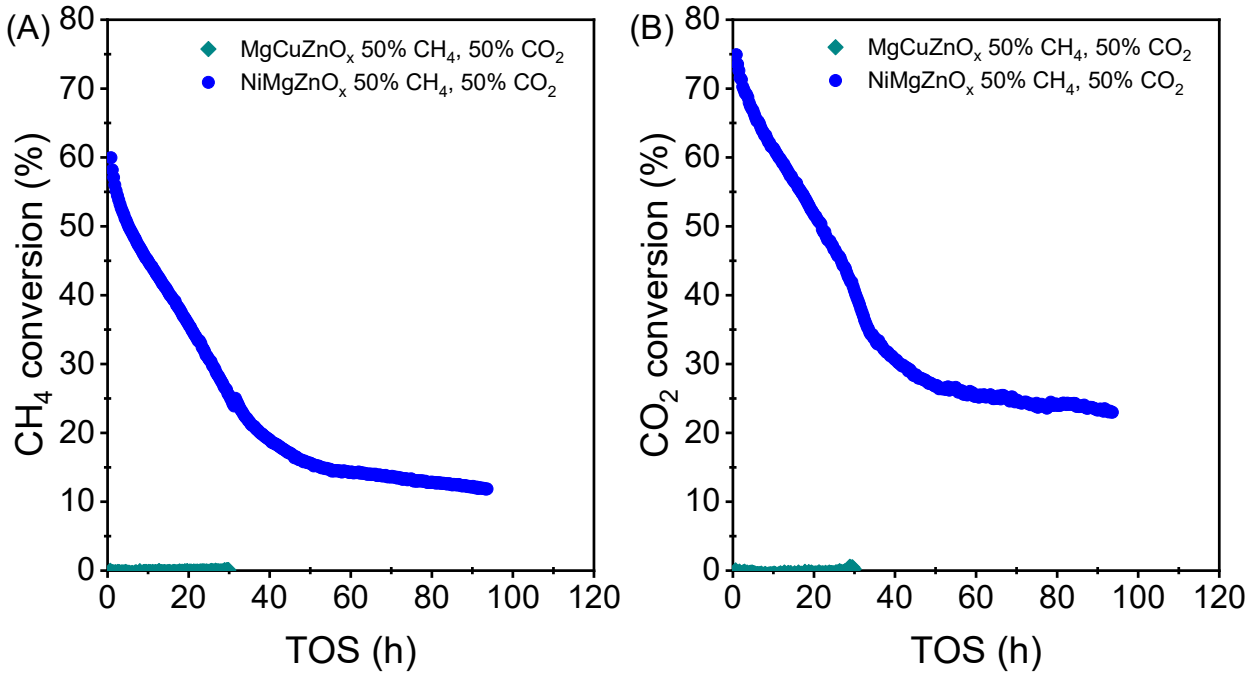

Figure S3. (A) CH_4 and (B) CO_2 conversion over $NiMgZnO_x$ and $MgCuZnO_x$ using concentrated feed (50% CH_4, 50% CO_2). DRM was conducted at 800 °C over 15 mg of catalyst. Prior to reaction, the catalyst was calcined at 900 °C and reduced at 800 °C at atmospheric pressure.

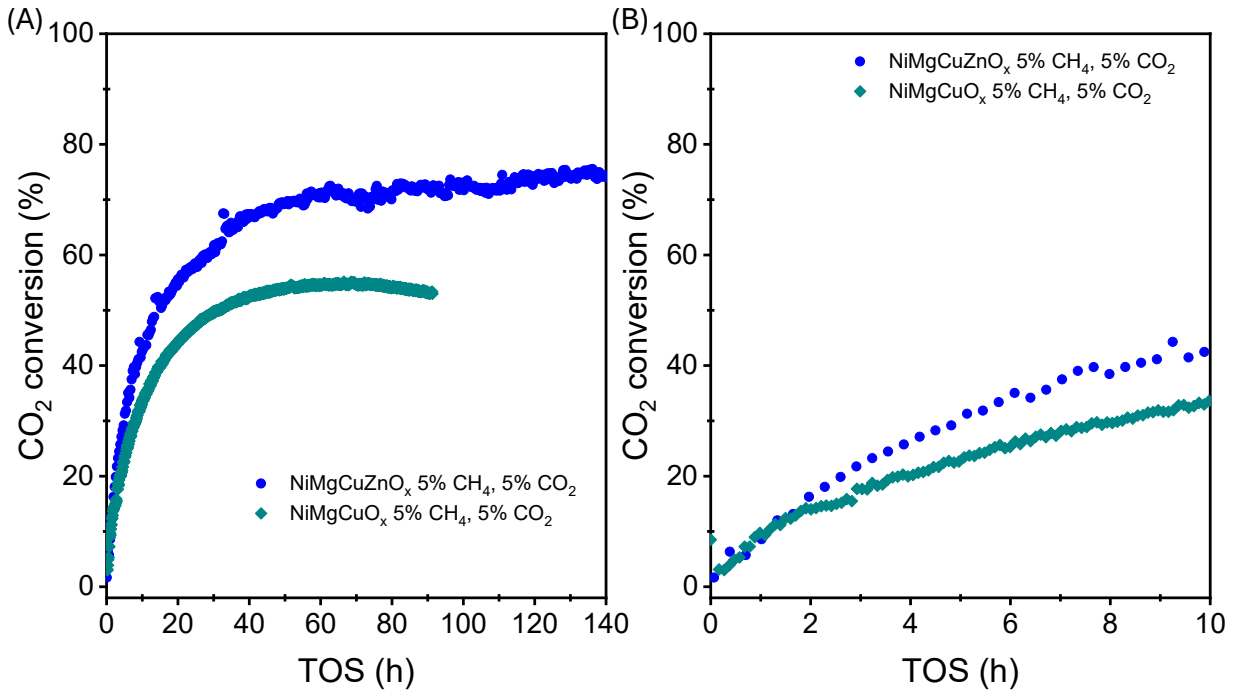

Figure S4. (A) CO_2 conversion of DRM over 15 mg NiMgCuZnO$_x$ and NiMgCuO$_x$ at 800 °C with mixture of 80 cm^3 50% CH_4 and 50% CO_2, and 80 cm^3 5% CH_4, 5% CO_2 balanced with Ar. (B) Zoom-in at low TOS.

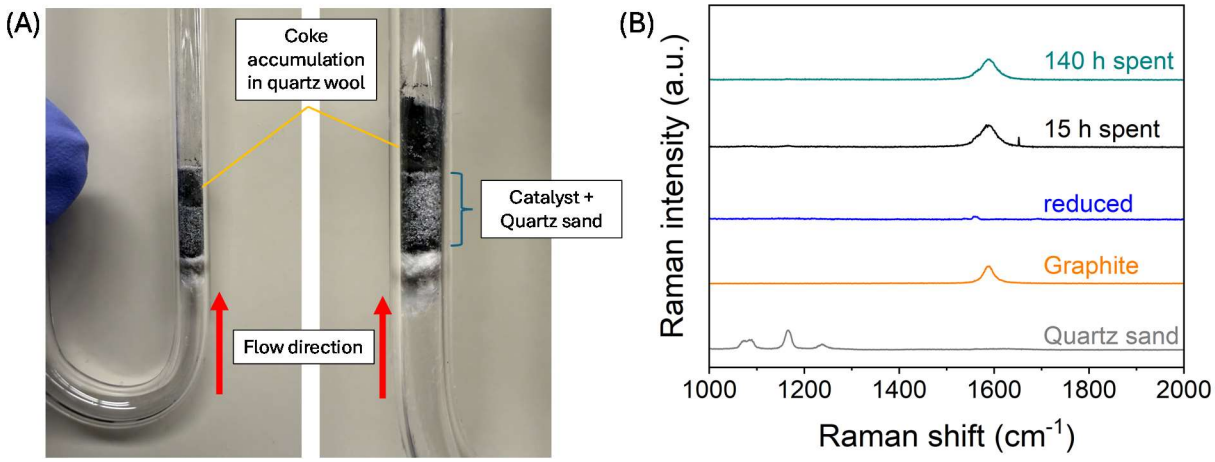

Figure S5. (A) Coke accumulated after DRM for 44 h TOS with 80 cm^3 of 50% CH_4 and 50% CO_2 at 800 °C over 15 mg of $NiMgCuZnO_x$. (B) Raman spectra of spent NiMgCuZnOx after 15 and 140 h of TOS during DRM reaction. Spectra from pretreated fresh catalyst, graphite and quartz sand are also shown for comparison.

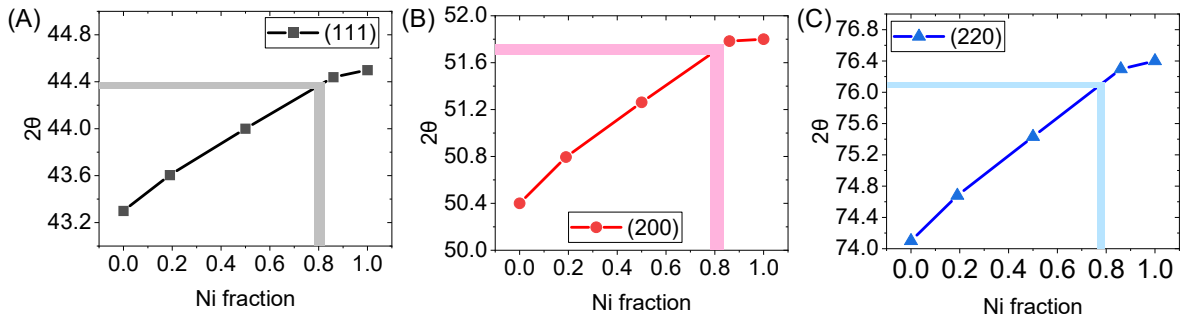

h	k	l	Ni	$Cu_{0.14}Ni_{0.86}$	$Cu_{0.5}Ni_{0.5}$	$Cu_{0.81}Ni_{0.19}$	Cu	$NiMgCuZnO_x$		
								red	15h	140 h
1	1	1	44.5	44.4	44.0	43.6	43.3	44.4	44.3	44.3
2	0	0	51.8	51.8	51.3	50.8	50.4	51.8	51.7	51.7
2	2	0	76.4	76.3	75.4	74.7	74.1	76.1	76.1	76.1

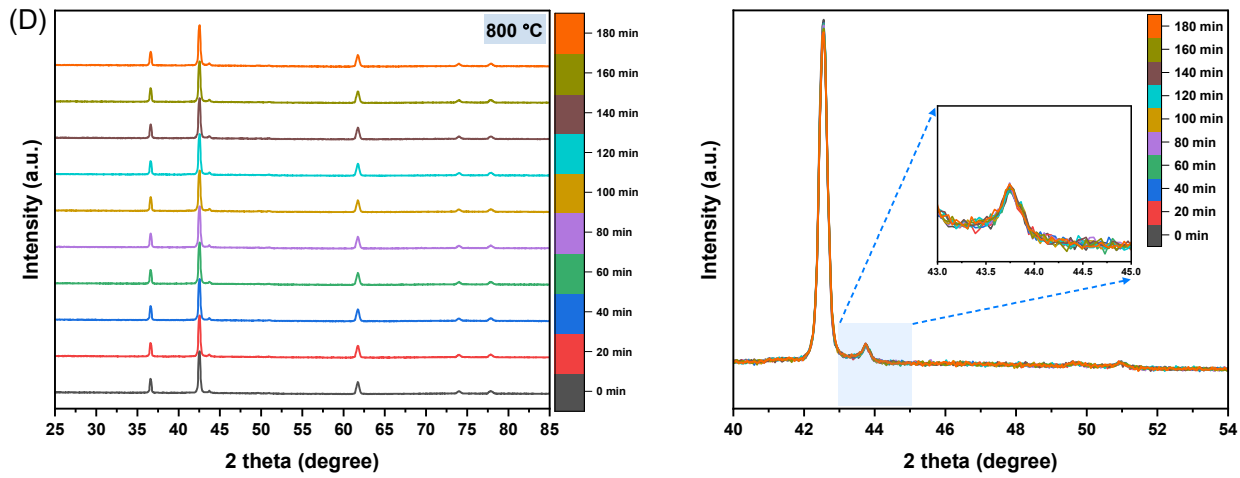

Figure S6. XRD diffraction peaks versus Ni fraction in Ni-Cu alloys. (A) (111) plane, (B) (200) plane, (C) (220) plane. (A-C) The interpolations (light gray, pink, and light blue line) represent diffraction peaks encountered in the spent NiMgCuZnOx samples as presented in the table. (D) In situ XRD of $NiMgCuZnO_x$ under DRM reaction conditions. The sample was pretreated ex situ in 5% O_2/He at 900 °C for 1 h, followed by pretreatment in 30% H_2/Ar at 800 °C for 5 h. Next, the sample was transported to the XRD chamber for in situ measurement. Data were continuously collected as the temperature was ramped at 40 °C/min to 800 °C and maintained at 800 °C for 180 min under a 0.5% CO_2/0.5%CH_4/He (150 cm^3/min) atmosphere.

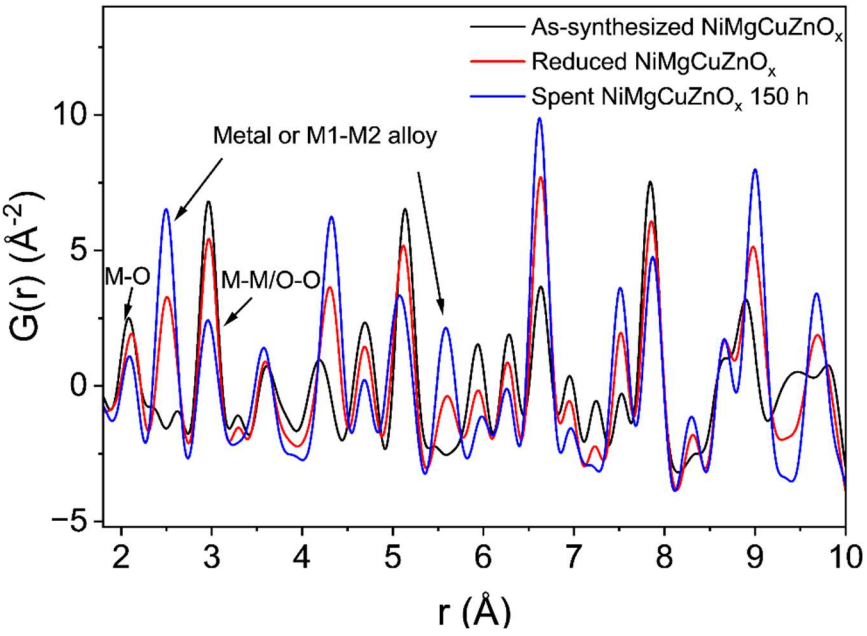

Figure S7. X-ray PDF of (A) as-synthesized NiMgCuZnOx and (B) NiMgCuZnOx after reduction and DRM reactions.

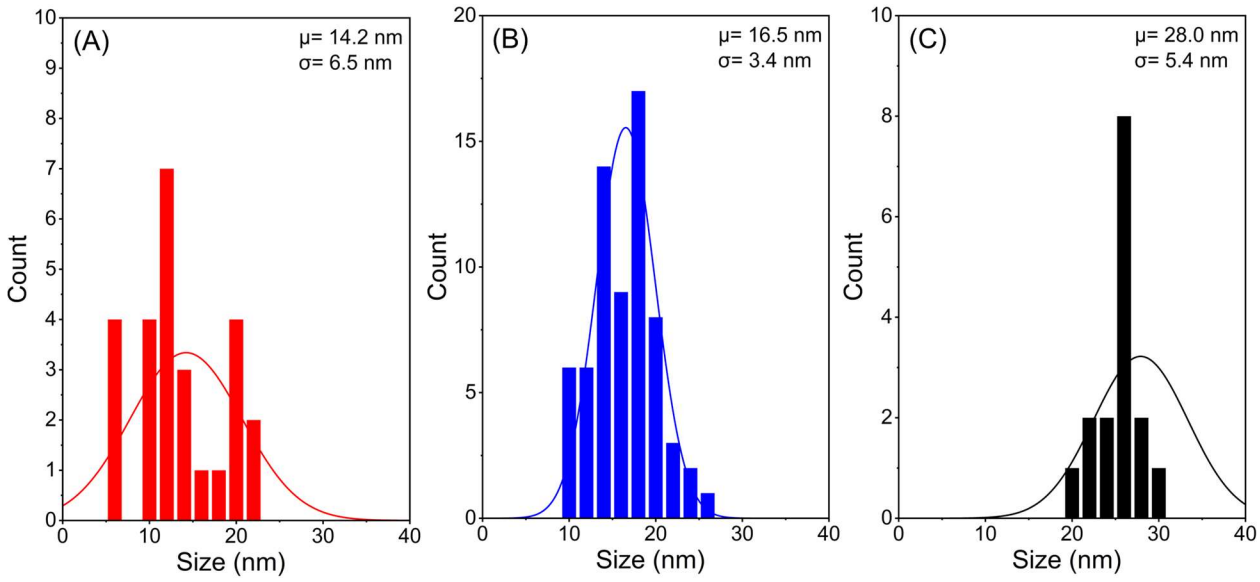

Figure S8. Particle size distribution of exsoluted nanoparticles in (A) reduced NiMgCuZnOx, spent NiMgCuZnOx after (B) 15 h and (C) 80 h DRM reaction.

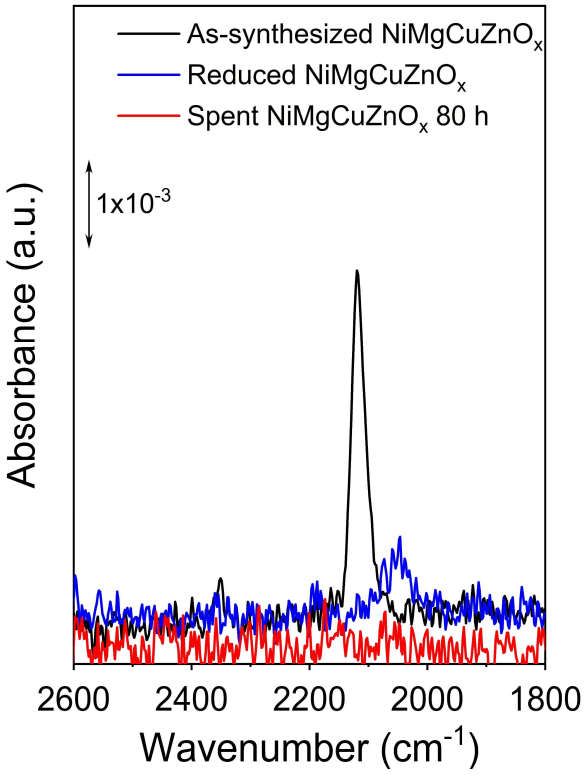

Figure S9. CO DRIFTS on as-synthesized, reduced and spent NiMgCuZnO$_x$. The spectra were measured at -100 °C after 5 min adsorption of 0.67% CO/He followed by 5 min desorption.

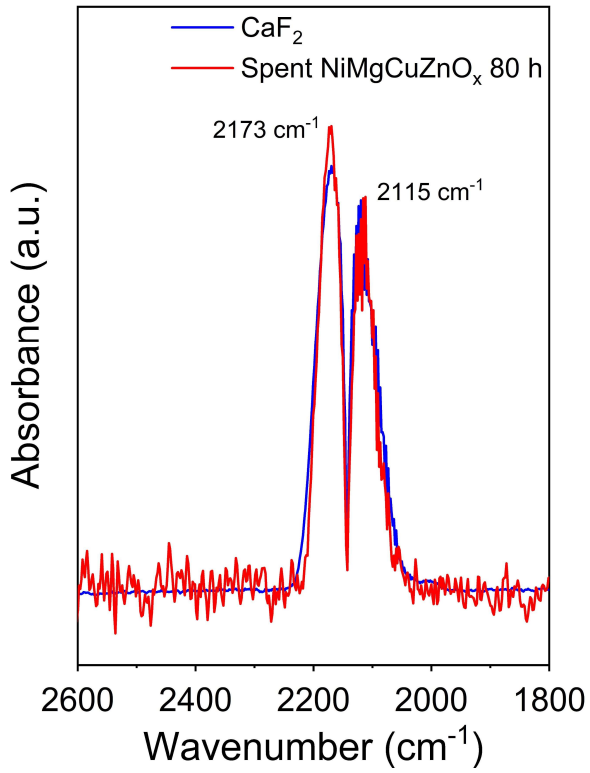

Figure S10. CO DRIFTS on spent $NiMgCuZnO_x$ and CaF_2. The spectra were measured at -100 °C after 5 min adsorption of 0.67% CO/He. The absorbance is normalized by peak at 2115 cm^{-1}.

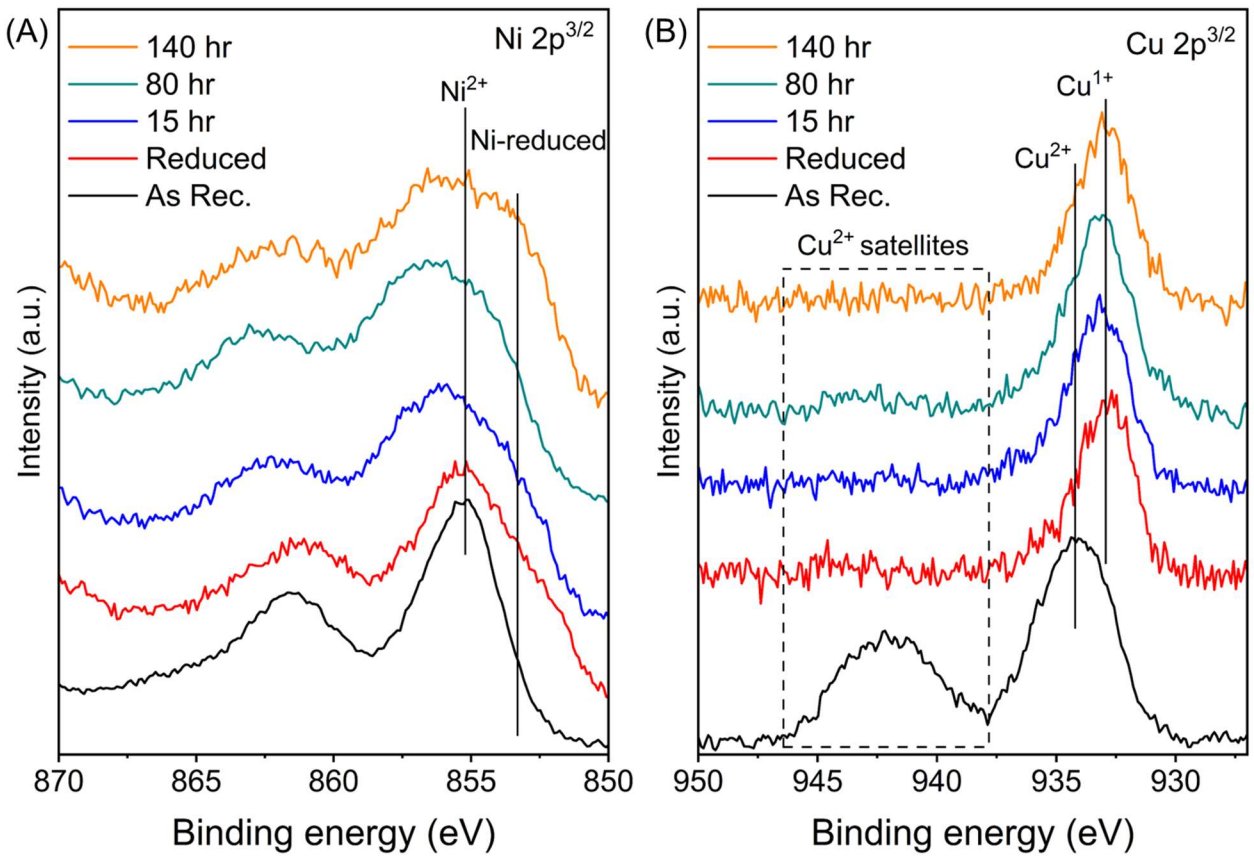

Figure S11. Ex situ (A) Ni 2p and (B) Cu 2p XPS spectra of as-synthesized, reduced and spent $NiMgCuZnO_x$.

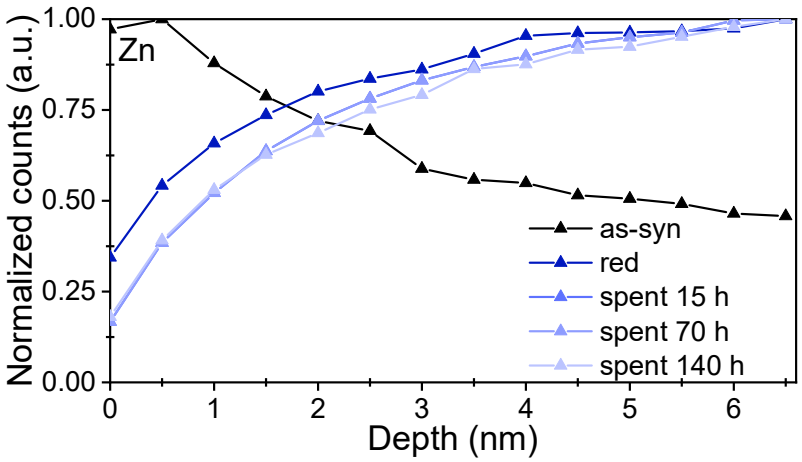

Figure S12. Ex situ LEIS Zn profiles of NiMgCuZnOx sample at different stages of catalytic performance measurement. “spent *X* h” refers to a spent catalyst during DRM at 800 °C for *X* h.

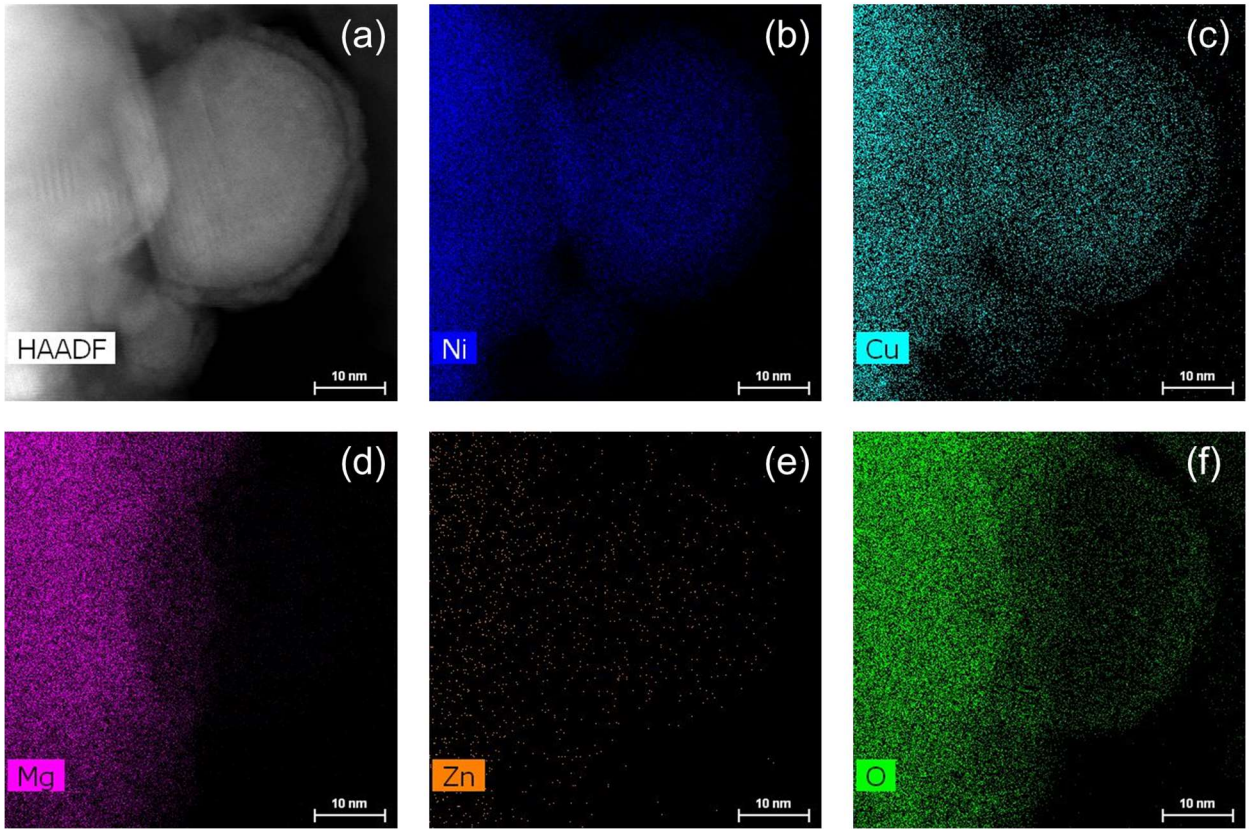

Figure S13. HAADF-STEM image and elemental mapping of spent $NiMgCuZnO_x$ sample after 15 h of TOS during DRM. “red” refers to calcination at 900 °C followed by reduction at 800 °C.

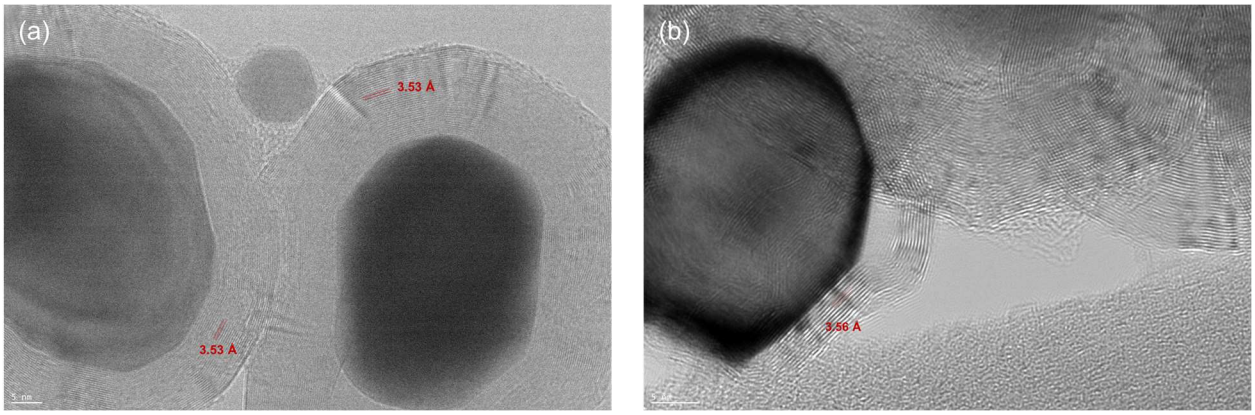

Figure S14. (HR) high-resolution transmission electron microscopy (HR-TEM) images of exsolved nanoparticles on spent NiMgCuZnOx after DRM at 800 C.

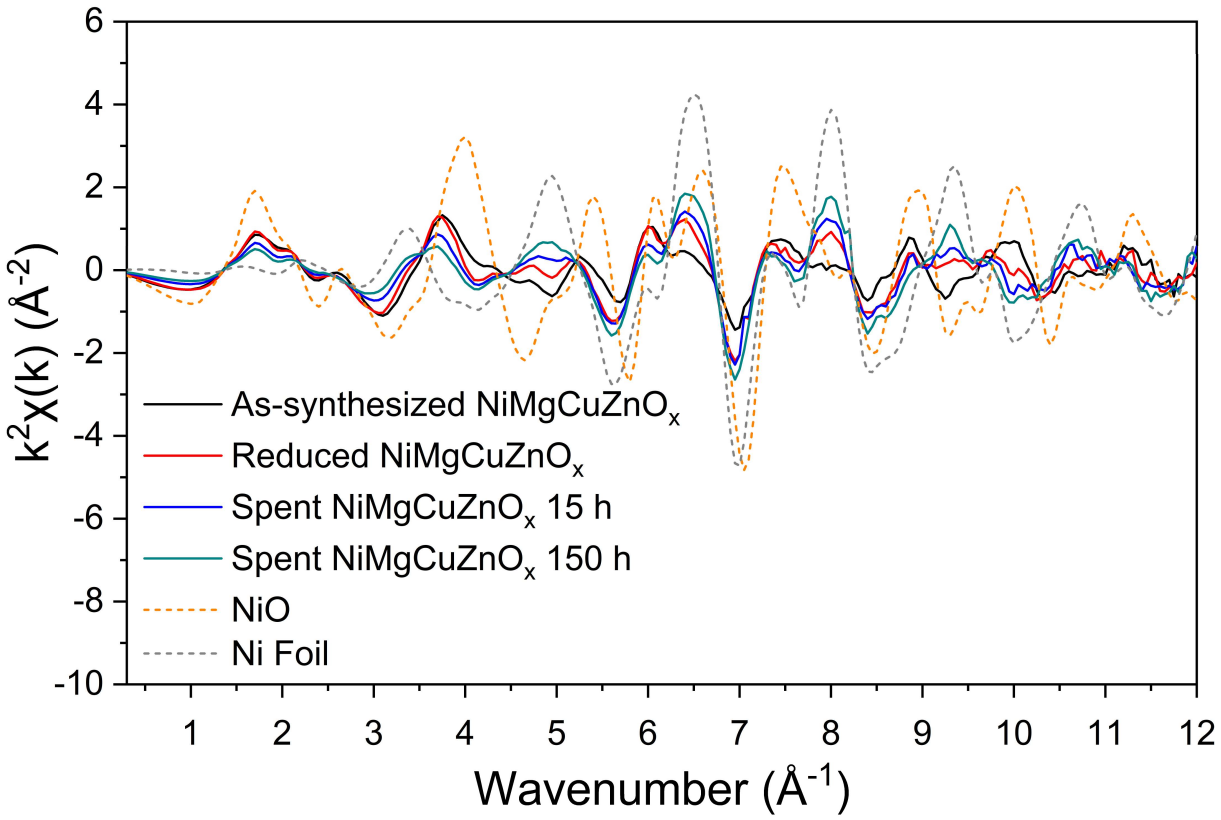

Figure S15. Ni K edge k-space EXAFS spectra of as-synthesized, reduced and spent samples with NiO and Ni foil reference.

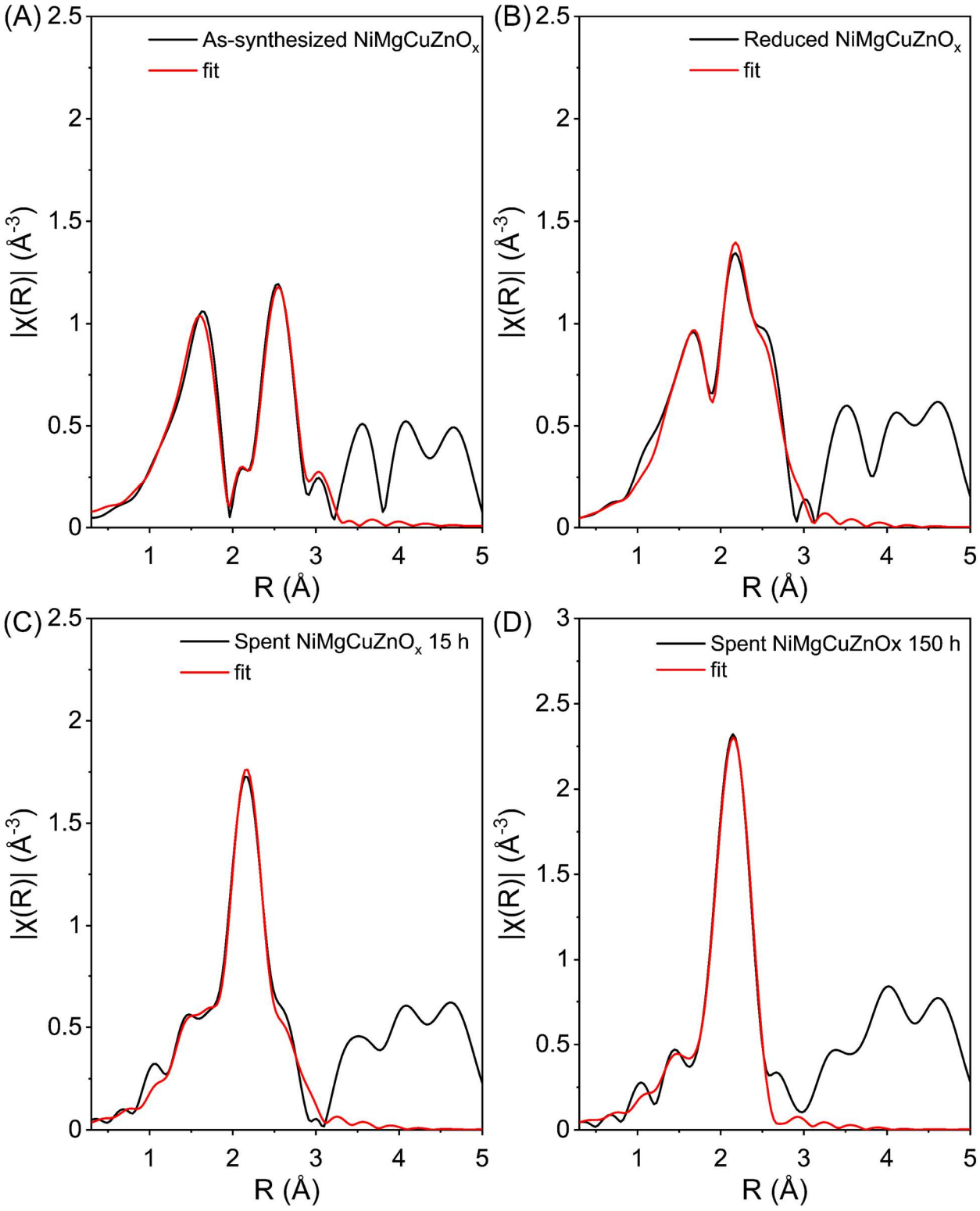

Figure S16. Ni K-edge R-space EXAFS spectra and model fits for (A) as-synthesized NiMgCuZnO$_x$, (B) reduced NiMgCuZnO$_x$, (C) spent NiMgCuZnO$_x$ after 15 h DRM reaction and (D) spent NiMgCuZnO$_x$ after 150 h DRM reaction.

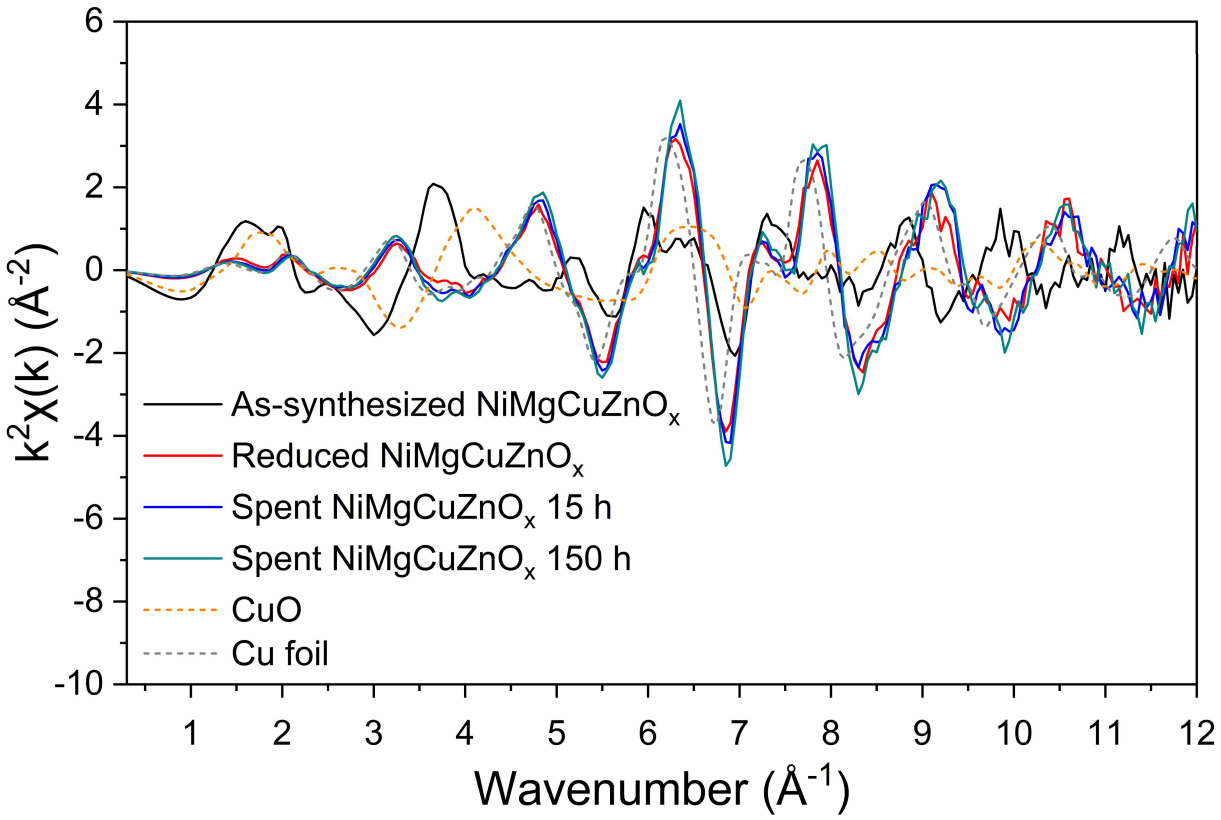

Figure S17. Cu K edge k-space EXAFS spectra of as-synthesized, reduced and spent samples with CuO and Cu foil reference.

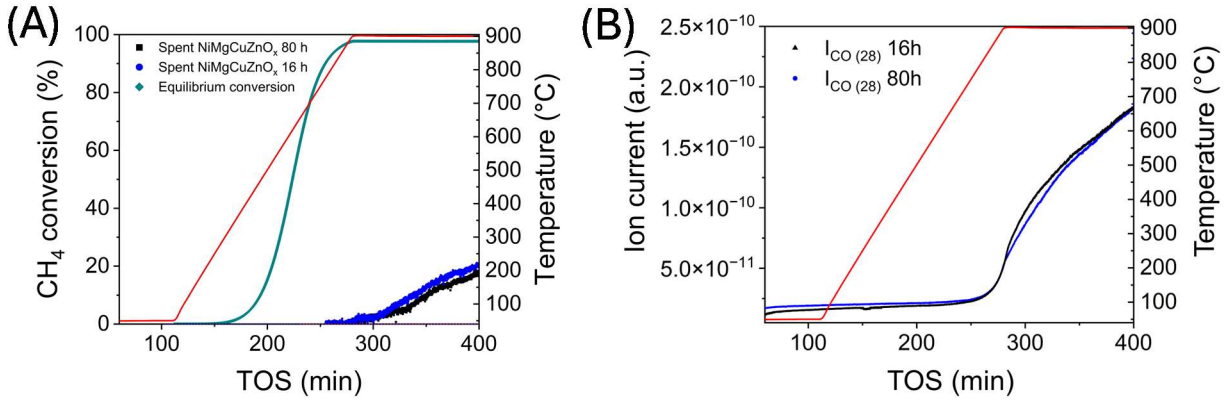

Figure S18. TPSR of 5% CH_4, 5% CO_2 on spent $NiMgCuZnO_x$ after 16 and 80 h DRM reaction. "Spent *X* h" refers to a spent catalyst during DRM at 800 °C for *X* h. (A) CH_4 conversion (B) CO evolution. $WHSV_{reactatns}$ = 96 $L.g_{cat}^{-1}$ h^{-1}.

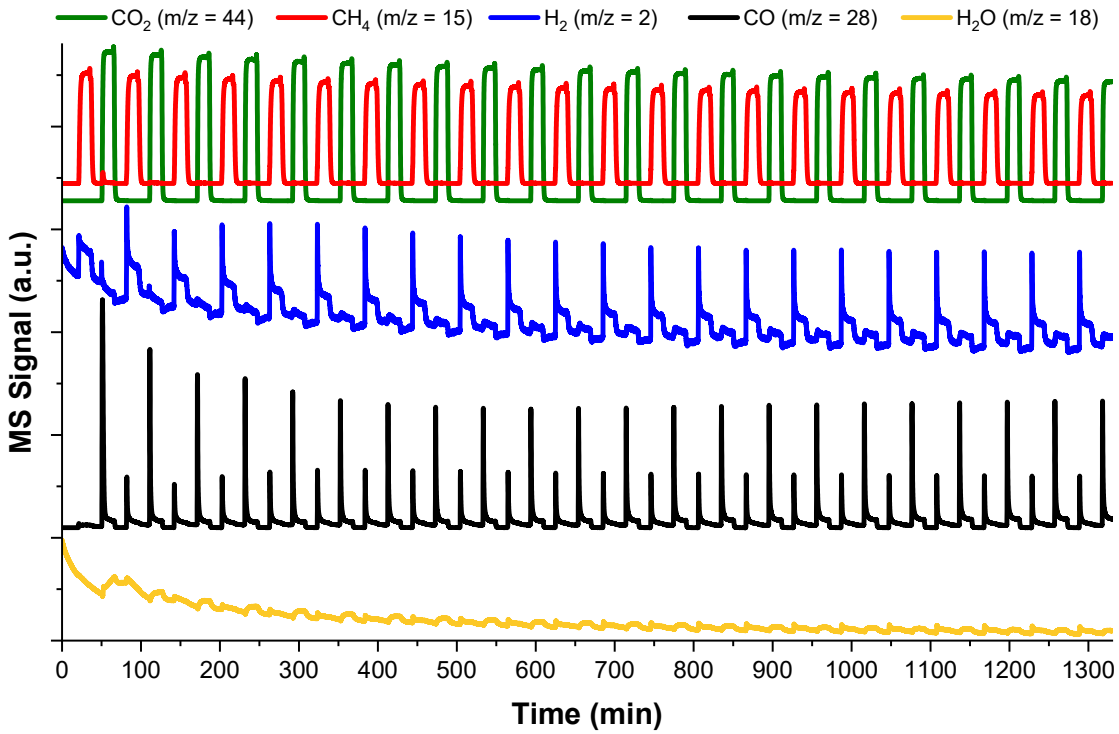

Figure S19. DRM Chemical looping at 800 °C. All cycles. $NiMgCuZnO_x$ catalyst was pretreated in O_2 at 900 °C and H_2 at 800 °C.

Table S1. ICP-AES characterization of catalysts.

Catalyst	Concentration (mol %, oxygen-free basis)			
	Ni	Cu	Zn	Mg
$NiMgCuZnO_x$ (as-synthesized)	31.3	18.5	1.21	49.0
$NiMgCuZnO_x$ (pretreated: O_2 900 °C, H_2 800 °C)	49.6	16.1	0.12	34.2
$NiMgCuZnO_x$ (after DRM at 800 °C for 30 h, 50 % CH_4, 50 % CO_2)	42.4	16.3	0.01	41.3
$NiMgCuO_x$ (as-synthesized)	29.0	7.6	0	63.4

Table S2. Ni K-edge EXAFS fitting results for $NiMgCuZnO_x$ samples and references.

Sample	Conditions	CN	Path	S_0^2	R (Å)	σ^2 ($Å^2$)	ΔE_0 (eV)	R factor
$NiMgCuZnO_x$	As-synthesized	2.7±0.2 3.0±0.3 4.1±2.7	Ni-O Ni-Ni Ni-O	0.99 0.99 0.99	2.057±0.01 2.971±0.009 3.59±0.04	0.005±0.001 0.005±0.001 0.01±0.01	-1±1	0.015
	reduced	2.8±0.5 3.1±0.9 3.0±0.7	Ni-O Ni-Ni Ni-Ni	0.99 0.99 0.81	2.10±0.02 2.93±0.03 2.50±0.01	0.006±0.002 0.006±0.002 0.006±0.002	4±2 -14±7 4±2	0.013
	Spent 15h	2.0±0.5 2.8±1.6 3.2±1.5	Ni-O Ni-Ni Ni-Ni	0.99 0.99 0.81	2.09±0.02 2.93±0.02 2.49±0.02	0.007±0.003 0.007±0.003 0.004±0.003	2±2 -14 2±2	0.005
	Spent 150h	1.7±0.9 6.3±1.0	Ni-O Ni-Ni	0.99 0.81	2.08±0.02 2.491±0.009	0.008±0.008 0.007±0.001	0±2	0.007
NiO		6 12 8	Ni-O Ni-Ni Ni-O	0.99±0.03	2.077±0.004 2.952±0.002 3.52±0.02	0.0063±0.0006 0.0063±0.0002 0.011±0.002	2.7±0.3	0.002
Ni foil		12	Ni-Ni	0.81±0.01	2.482±0.001	0.0060±0.0001	-0.1±0.2	0.001

Table S2. Cu K-edge EXAFS fitting results for $NiMgCuZnO_x$ samples and references.

Sample	Conditions	CN	Path	S_0^2	R (Å)	σ^2 ($Å^2$)	ΔE (eV)	R factor
$NiMgCuZnO_x$	reduced	10.7±1.0	Cu-Cu	0.91	2.509±0.004	0.0075±0.0007	-3.7±0.5	0.005
	Spent 15h	10.9±1.0	Cu-Cu	0.91	2.503±0.003	0.0070±0.0007	-3.7±0.5	0.005
	Spent 150h	12.0±0.9	Cu-Cu	0.91	2.502±0.003	0.0071±0.0006	-3.7±0.5	0.005
Cu foil		12	Cu-Cu	0.91±0.02	2.543±0.002	0.0087±0.0002	-3.2±0.3	0.001